PNAS RESEARCH ARTICLE | EARTH, ATMOSPHERIC, AND PLANETARY SCIENCES

Asymmetric and Intermittent Supershear Rupture Mediated by Local Fault Complexity during the 2025 M_W 7.7 Myanmar Earthquake

Tao Xia[a], Lingling Ye[a,1], Jinlai Hao[b], Haijun Gao[a], Thorne Lay[c], Xiaotian Ding[a], and Zhenxing Yao[b]

Affiliations are included on p. 10.

Edited by John Vidale, University of Southern California, Los Angeles, CA; received January 25, 2026; accepted June 12, 2026

We determine the detailed rupture process of the 2025 M_W 7.7 Myanmar earthquake by joint inversion of near-fault strong-motion, geodetic, and teleseismic data. The rupture initiated with significant slip of up to ~5 m near the epicenter. Localized fault geometric complexity and stress heterogeneity might have led to small-scale slip segmentation and intermittent episodes of supershear rupture. Northward rupture propagation was subshear overall and terminated rapidly after extending ~80 km within the partial stress shadow of a 2012 earthquake. In contrast, southward rupture propagated ~380 km, fully traversing a predefined seismic gap that had been unruptured since 1839, and undergoing cycles of acceleration and deceleration that included at least two episodes of intermittent supershear rupture before gradually stopping after traversing a segment that ruptured in 1930. Slip exceeding 3 m is confined to the shallow fault above a 15 km locking depth and the average static stress drop is 4.7 MPa. The long-term stress accumulation on multiple asperities along the central Sagaing fault promotes localized ruptures in discrete events but sometimes leads to rupture cascades with intermittent supershear behavior as in 2025. Local slip duration also displays a north–south asymmetry, being longer near the epicenter and progressively shorter toward the south before the end. This pattern may be associated with lower rigidity near the epicenter and rupture dynamics being modulated by fault edges for long, narrow strike-slip faults. Our findings highlight the roles of localized fault structure and stress heterogeneity in controlling slip distribution and rupture speed.

myanmar earthquake | asymmetric rupture | intermittent supershear | geometric complexity | stress heterogeneity

Significance

Intermittent supershear rupture (rupture propagating faster than the local shear-wave speed, enhancing ground shaking) has infrequently been documented for natural earthquakes, mainly due to the scarcity of dense near-fault observations. Using multiple complementary datasets, we resolve that the ~480-km-long 2025 Myanmar M_W 7.7 earthquake exhibits north–south asymmetry with long-duration slip near the epicenter and at both ends, and short-duration slip with a higher slip rate in the center. We find that localized along-strike variations in fault geometry might strongly mediate the rupture dynamics, including north–south asymmetry, intermittent supershear rupture, and small-scale slip segmentation. Our results highlight the need to enhance the availability of near-fault measurements to resolve the complexity of dynamic ruptures and to advance our understanding of earthquake physics.

On March 28, 2025, an M_W 7.7 earthquake struck central Myanmar, causing severe casualties and damage, particularly in Nay Pyi Taw and Mandalay (Fig. 1). The event occurred on the Sagaing Fault, a 1,200 km long right-lateral strike-slip fault that forms part of the boundary between the Burma microplate and the Sunda plate (Fig. 1*A*). As one of the world's longest and most active strike-slip faults (1–3), it has a relatively simple and continuous fault geometry for the ~700-km-long central section. Despite its overall continuity, the fault comprises multiple segments, delineated mainly by localized fault geometric complexity, including bends, stepovers, and branching structures [Fig. 1*A*; (4, 5)]. Each segment has historically generated earthquakes of magnitude larger than ~7, while the Meiktila segment has remained unruptured since 1839, and was recognized as a seismic gap [Fig. 1*B*; (6)]. Relatively extensive near-fault observations from space geodesy and seismic observations are available for the 2025 Myanmar earthquake, although strong-motion sensors are more limited than those available for the 2023 Türkiye earthquakes (7–9), and joint analysis of available data provides details of the rupture process.

Previous studies have analyzed the rupture process of the 2025 Myanmar earthquake rupture process using single or multiple observations and techniques. Studies consistently indicate a bilateral rupture, with the southern rupture extending ~400 km and the northern rupture ~100 km, but vary significantly in rupture details and inferred local rupture propagation speeds (e.g., refs. 13–29; *SI Appendix*, Fig. S1). Two near-fault observational sites recorded the local ground motion history for this earthquake. A CCTV camera, located less than 100 m from the fault, captured visual images of local subshear rupture (17, 27), while the NPW strong-motion station 2.6 km from the fault captured stable broadband ground motions and static offsets indicating supershear rupture with average rupture propagation speed of 4.8 km/s (14). The waveform characteristics of fault parallel and normal motions provide direct constraints on local rupture speeds at this site (28). However, a consensus has yet to be reached on the nature of the southern supershear rupture (*SI Appendix*, Fig. S2).

The authors declare no competing interest.

This article is a PNAS Direct Submission.

PNAS policy is to publish maps as provided by the authors.

[1]To whom correspondence may be addressed. Email: yell@sustech.edu.cn.

This article contains supporting information online at https://www.pnas.org/lookup/suppl/doi:10.1073/pnas.2602650123/-/DCSupplemental.

Published July 6, 2026.

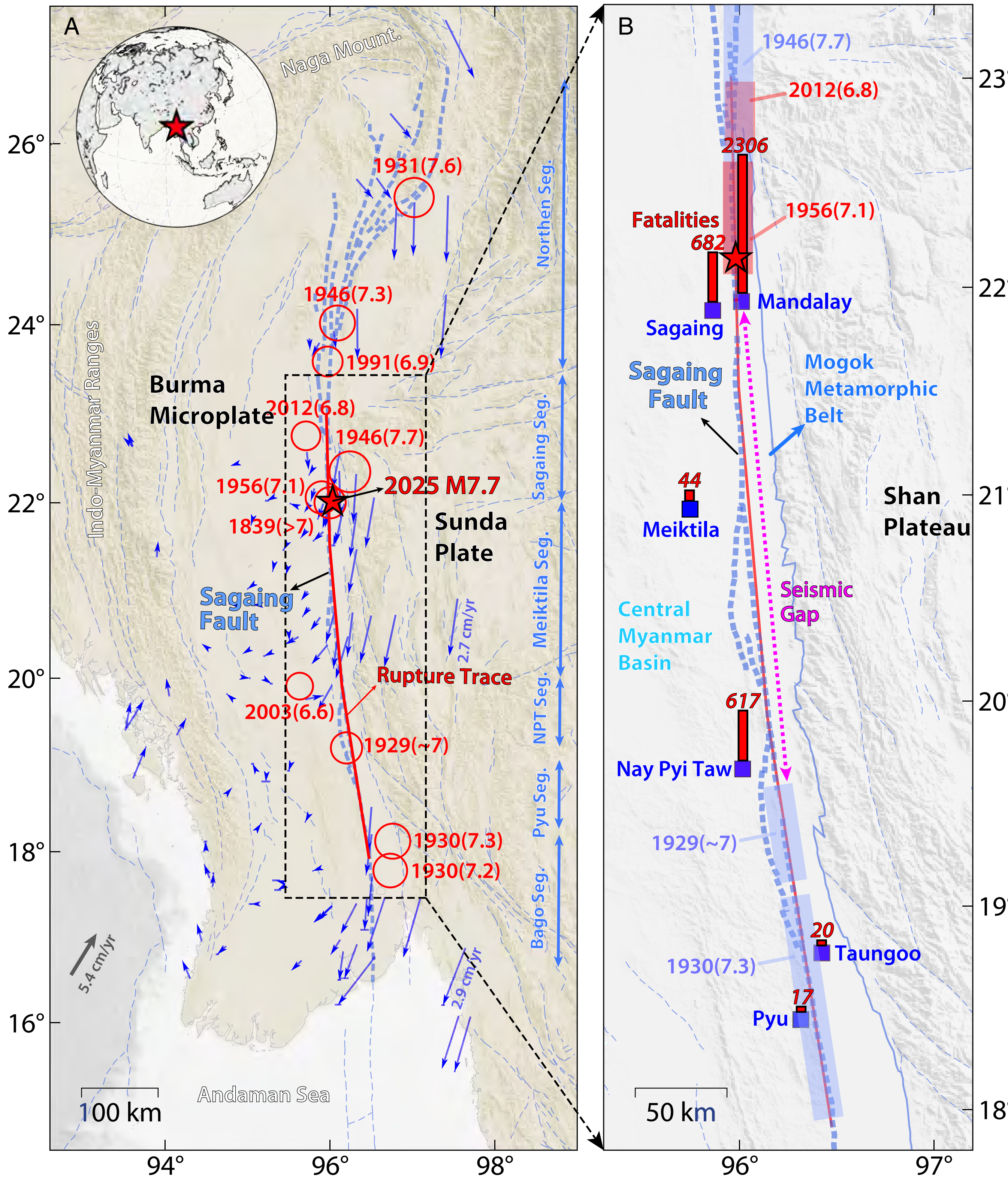

Fig. 1. (*A*) Tectonic setting around the 2025 Myanmar earthquake. Blue arrows indicate plate motions relative to the Burma microplate (10). Red circles mark historical earthquakes from Wang et al. (4), and the star denotes the epicenter of the 2025 M_W 7.7 Myanmar earthquake (11). Bold blue dashed lines show the Sagaing fault system. Red solid line is the surface rupture trace of the 2025 Myanmar earthquake along the Sagaing fault of the 2025 Myanmar earthquake. The fault segments are labeled on the right side of the map. (*B*) Historical earthquake ruptures and geological units along both sides of the Sagaing Fault. The eastern side is the Mogok Metamorphic Belt, while the western side is the Central Myanmar Basin (5). The central segment without recent ruptures corresponds to the previously defined seismic gap zone (6). The rupture zones of historical earthquakes are from Wang et al. (4). Dark blue boxes indicate major cities located along the fault, along with red bars showing the fatalities from the 2025 Myanmar earthquake (12).

Some studies suggest that it propagated as a mostly sustained supershear rupture with brief subshear intervals (21, 22, 25) or in a fully sustained supershear rupture (26), while others indicate an intermittent behavior, with multiple alternating phases of supershear and subshear (14, 17, 24). For the northern rupture, there is also some disagreement, with some studies reporting supershear rupture

(13, 23) while most others infer predominantly subshear rupture (e.g., refs. 14, 19, 26).

Large continental strike-slip earthquakes commonly exhibit complex static slip distributions and variations in rupture speed along the fault, both of which can be strongly influenced by fault geometry and stress heterogeneity (30–34). In particular, rupture speed may enter the supershear regime, where the rupture front propagates faster than the local shear wave, potentially causing severe damage from the resulting shock wave. Numerical simulations, laboratory experiments, and limited field observations indicate that the initiation and propagation of supershear rupture can be influenced by multiple factors, such as the bimaterial effect across the fault (35, 36) and free surface effects (37). These factors can control whether supershear rupture propagates in a sustained way (38, 39) or exhibits intermittent behavior (7, 32, 34, 40). However, due to the lack of dense near-fault observations, evidence of the intermittent supershear rupture remains limited for natural earthquakes.

Motivated by these conflicting results from prior studies and observations, we aim to address the following questions regarding the 2025 Myanmar earthquake: 1) whether the slip distribution exhibits localized segmentation affected by local fault geometric complexities; and 2) whether the rupture speed evolution involves intermittent or sustained supershear pattern. To answer these questions, we jointly analyze available near-fault strong-motion records, geodetic observations, and teleseismic data to construct a detailed rupture model of the earthquake. We then focus on the along-strike variations in the slip distribution and rupture speed assessing how these features correlate with local fault geometry and stress conditions.

Surface Deformation Revealed by Geodetic Observations. The multiview coseismic surface deformation field observed by satellite geodesy (Fig. 2), including Sentinel-2A optical, ALOS-2, and Sentinel-1A Synthetic Aperture Radar (SAR) images (*SI Appendix*, Tables S1 and S2), indicates that the 2025 Myanmar earthquake produced a surface rupture of ~480 km along the Sagaing Fault, with deformation dominated by right-lateral strike-slip motion. Geodetic measurements from four independent viewing geometries consistently reveal pronounced along-strike variations in surface deformation, a pattern that is particularly evident in the ALOS-2 deformation field (Fig. 2*A*) and optical images (Fig. 2*B*).

Along the Sagaing fault, the main surface deformation from north to south can be divided into three prominent segments located near the epicenter, approximately 120 km south of the

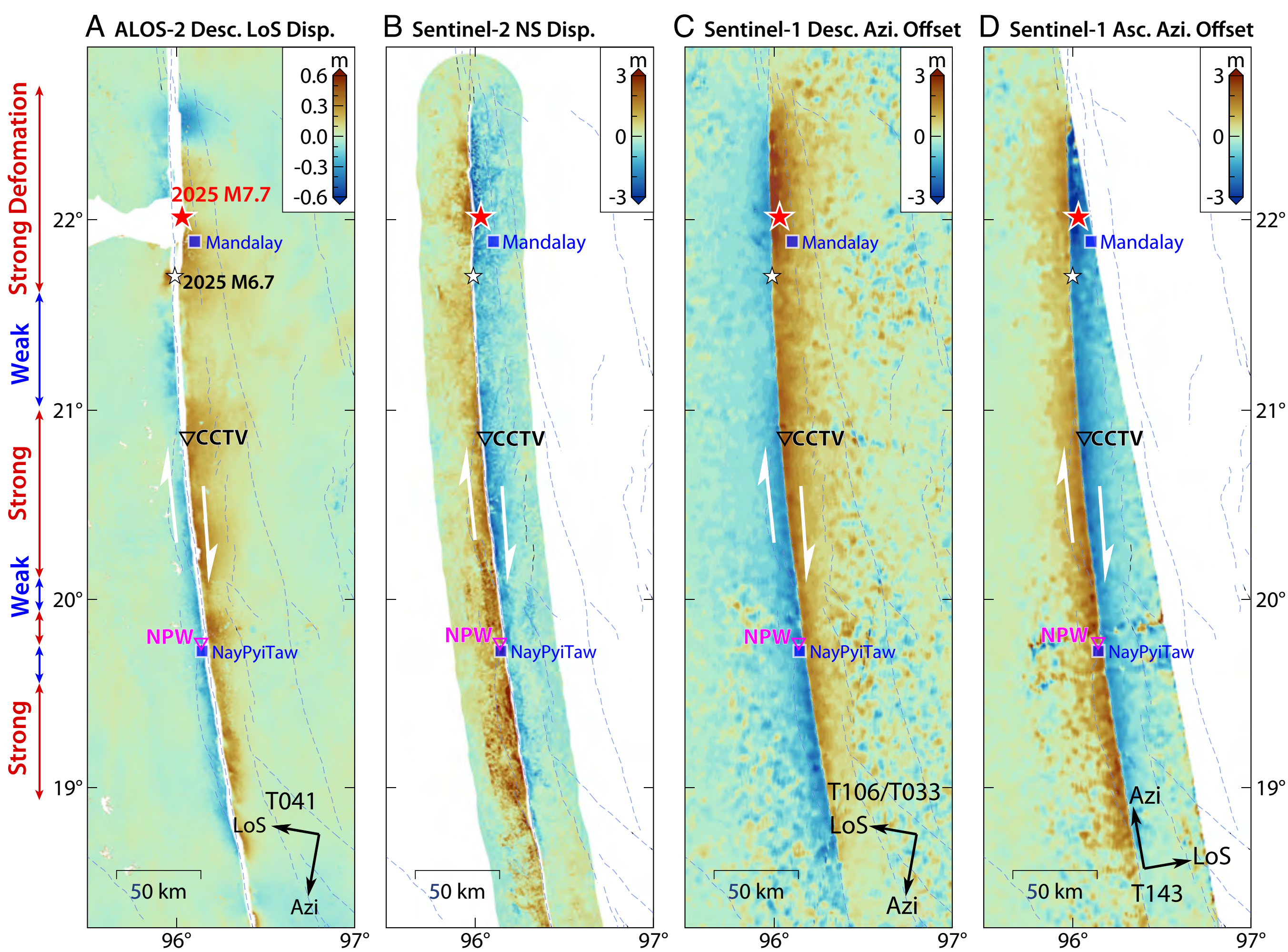

Fig. 2. Coseismic deformation fields of the 2025 Myanmar earthquake derived from multiple geodetic datasets. (*A*) Descending line-of-sight (LoS) displacements from differential interferometric ALOS-2 T041 SAR images. (*B*) North–south (NS) displacements from subpixel correlation of Sentinel-2 optical images. (*C*) Descending azimuth offsets from pixel offset tracking (POT) of Sentinel-1 T106 and T033 SAR images. (*D*) Ascending azimuth offsets from POT of Sentinel-1 T143 SAR images. Red and white stars mark the epicenters of the 2025 Myanmar mainshock and M6.7 aftershock (11, 41), respectively. White arrows indicate the relative motion across the Sagaing fault. Blue squares denote major cities along the fault. The purple triangle marks the NPW strong-motion station located ~2.6 km away from the fault. The black triangle indicates the location of a CCTV camera. *Left* arrows highlight the segmented strong-weak-strong deformation pattern in the displacement fields with red and blue for strong and weak deformation, respectively.

epicenter, and in the region south of the NPW strong-motion station. The largest surface displacement, reaching ~5 m, occurred near the epicenter, where both the deformation amplitude and area on the eastern side of the fault are significantly greater than those on the western side. From north to south, the deformation range on the eastern side of the fault gradually decreases, while that on the western side progressively increases. About 50 km south of the epicenter, a relatively weak deformation segment emerges (amplitude of <0.1 m in ALOS-2 and <1 m in Sentinel-2 deformation fields), characterized by substantially smaller displacements on both sides of the fault. Farther south, a relatively continuous zone of strong deformation extends for ~150 km, from south of the CCTV site to north of the NPW strong-motion station. Near NPW, this continuous deformation is interrupted by a relatively weakly deformed section with approximately 30 km length, followed by the reappearance of a major slip zone south of NPW where the deformation amplitude and the spatial extent become comparable on the two sides of the fault. This transition in deformation distribution may in part reflect a systematic increase in fault dip from north to south along the strike. However, differences in rigidity between the northern and southern segments of the Sagaing fault may also contribute to this observed asymmetry (20).

Slip Distribution Jointly Inverted from Multiple Datasets. The preferred finite-fault slip model constrained by the multiple datasets (Fig. 2 and *SI Appendix*, Figs. S3–S5 and Tables S3 and S4) is shown in Fig. 3*A*. Fault motion is dominated by right-lateral strike-slip, with a minor component of dip-slip motion. The total seismic moment is 4.51×10^{20} Nm, corresponding to a moment magnitude of M_W 7.70. The maximum slip is approximately 5 m located near the epicenter. Slip exceeding 3 m is mainly concentrated at depths less than 15 km, consistent with the locking depth inferred from Global Navigation Satellite System (GNSS) observations (10). Following the method of (42), we estimate a slip-weighted average static stress drop of 4.7 MPa from the preferred slip model using Okada's Green functions (43). The slip distribution along the strike is overall smooth and continuous, with local slip gaps, resulting in a multisegment pattern consistent with geodetic observations. Segment F1 is characterized by large and spatially extensive slip, reaching ~5 m. Segment F2 is marked

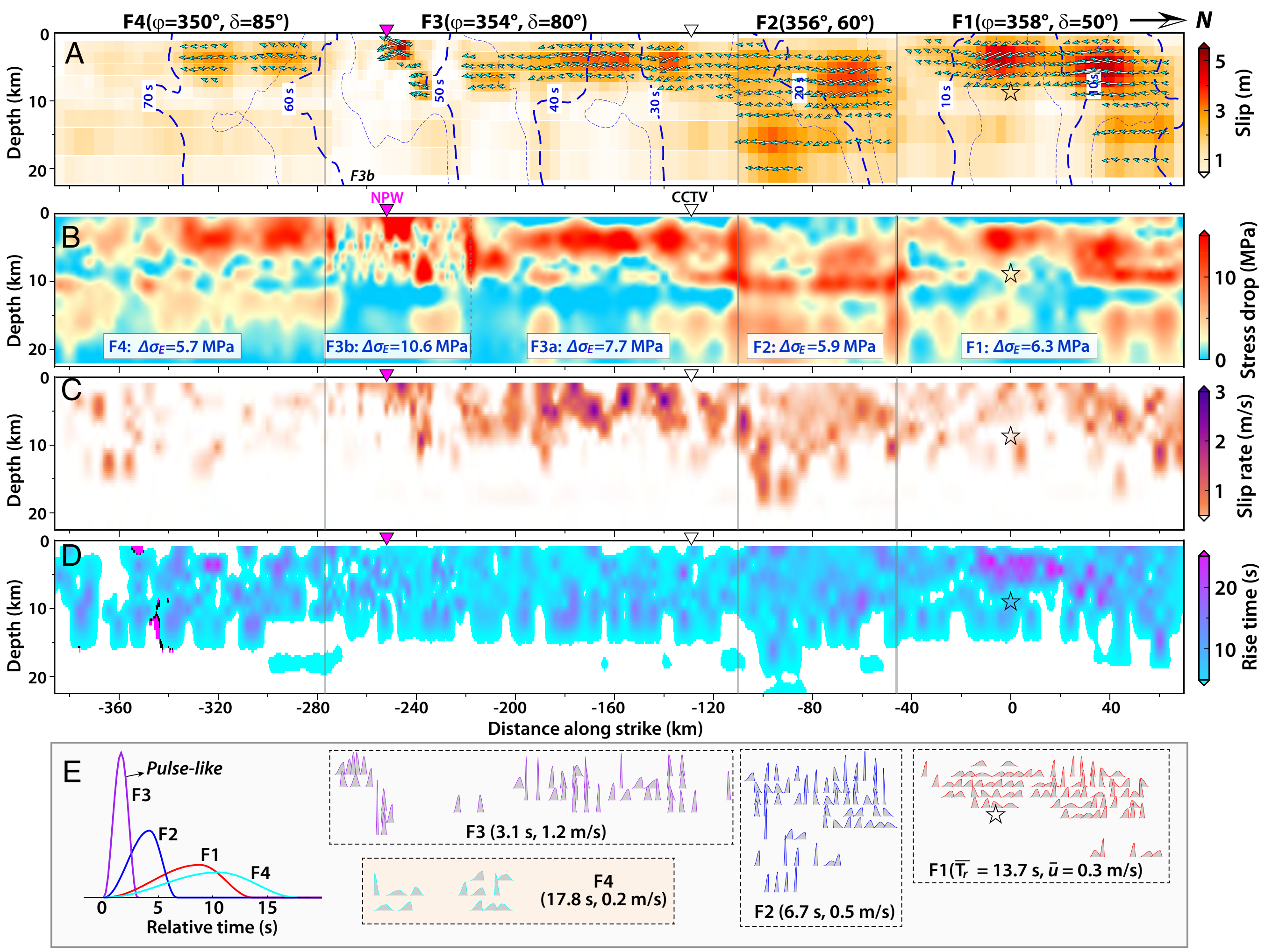

Fig. 3. Coseismic slip model of the 2025 Myanmar earthquake. (*A*) Slip distribution with arrows showing the magnitude and direction of slip (east side relative to west side) and subfaults color-coded by peak slip. The strike and dip angles for each fault segment are noted at the top. Black star indicates the hypocenter. Magenta and black triangles show the location of station NPW and the CCTV camera along the Sagaing fault, respectively. (*B*) Stress drop. The average stress drop calculated from the slip distribution shallower than 10 km are noted at the bottom of each fault segment. (*C*) Slip rate distribution of the preferred slip model. The slip rate is the ratio of fault slip to rise time. (*D*) Rise time distribution of the preferred slip model. (*E*) The *Left* panel shows the average source time functions (STF) for different segments, and the *Right* panels show the STFs for subfaults of each fault segment. The segment F4 is shifted for clarity. For each segment, the average slip duration $\overline{T_r}$ and average slip rate $\overline{u}$ are annotated. Different colors denote different segments. To clearly illustrate STF shapes, the time and amplitude scales are not uniform across segments. The average STF, $\overline{T_r}$ and $\overline{u}$ are calculated using only subfaults with slip greater than 2 m.

by shallow slip peaking at ~4 m 50 km south of the epicenter, with minor slip at depth, and farther south (80 to 100 km) shallow slip decreases to ~2 m while deep slip reaches ~3 m at ~15 km depth. Segment F3a shows relatively small slip (~1 to 2 m) north of the CCTV site, while south of the CCTV site, the slip becomes more continuous and smoother, reaching ~4.5 m. Segment F3b exhibits localized slip near station NPW (~250 km south of the epicenter), with a maximum of ~5 m over a smaller spatial extent than near the epicenter. The slip between segments F3b and F4 is reduced over a 30 km long zone (250 to 280 km south of the epicenter). Segment F4 resumes slip southward from ~280 km, extending ~50 km with a maximum of ~3 m.

Checkerboard tests (*SI Appendix*, Figs. S6 and S7 and *Text S1*) demonstrate that our inversion, constrained by multiple observations, can accurately recover the location and amplitude of the main slip areas. Teleseismic waveforms are particularly sensitive to deep slip, strong-motion waveforms near the fault better constrain local slip in the vicinity of the recording stations regardless of depth, and geodetic data most effectively resolve shallow slip. Joint inversion of all datasets (*SI Appendix*, Figs. S6*E* and S7*E*) provides the best model recovery. Sensitivity tests on segment F1 show that increasing the dip from 50° to 70° degrades the fit to the initial teleseismic *P*-waves (*SI Appendix*, Fig. S8), indicating that the fault near the epicenter likely has a relatively low dip of ~50°, in agreement with (14, 20), and supporting the geometry of the preferred model. Moreover, five inversions with different initial model seeds but identical inversion parameters produce a consistent mean slip model with low standard deviation, indicating stable and well-resolved slip features (*SI Appendix*, Fig. S9). Importantly, the preferred slip model reproduces both SAR and optical deformation fields, teleseismic waveforms, and near-fault strong-motion waveforms well, demonstrating its overall viability (*SI Appendix*, Figs. S10–S17), and setting this study apart from earlier work. We used an average 1D velocity structure in the inversion, which is not realistic for the ~480-km-long rupture and might have introduced artifacts into the preferred slip model. Therefore, we focus on the key features well constrained by the observations in the following discussion.

In addition to the slip segmentation, variations in rupture duration near the epicenter and on southern segments indicate a multistage rupture process. In the first 10 s, subfaults near the epicenter have slip durations exceeding 20 s, whereas subfaults 20 km to the north and south show durations generally below 8 s (Fig. 3*D*). The source time functions of the subfaults indicate pulse-like rupture on F2 and F3, consistent with the high slip rate, whereas F1 exhibits a longer duration and relatively low slip rate (Fig. 3 *D* and *E*). The CCTV camera located less than 100 m from the fault captured the local rupture 120 km south of the epicenter, showing cumulative slip of ~3 m with a duration of 1.4 s, and peak slip rates of 3.5 m/s (27, 44). The preferred slip model without using the CCTV data reproduces slip durations of less than 10 s and slip rates of 2 to 3 m/s at this location (Fig. 3 *C* and *D*), comparable to the observed data at the CCTV site. Although the inverted slip rates and durations at the CCTV site are affected by grid size, parameter settings, and data resolution, the overall magnitudes and general patterns remain consistent with the observations, supporting the validity of the preferred slip model. Comparison of our preferred slip model and previously published models (*SI Appendix*, Fig. S1) shows significant differences arising from the use of different datasets and inversion methods. Our preferred model fits all of the data used very well with less pronounced slip variations than other studies. Several spatial smoothing factors (0.1, 0.3, 0.5, and 0.7) were tested, and the preferred model with the smoothing factor of 0.5 was selected based on a balance between fitting the observations and model smoothness (*SI Appendix*, Fig. S18).

Slip Segmentation Controlled by Structure and Stress. Slip segmentation in large continental strike-slip earthquakes is often associated with the uneven accumulation of interseismic stress and the structural complexity of the fault system (45, 46). Geometric features, such as fault steps and bends, can result in local stress concentrations, promoting or inhibiting slip propagation and termination, thereby shaping the final slip distribution (47, 48). To quantify fault complexity, Chu et al. (49) proposed the fault misalignment (R_M), which evaluates the strike variation within a fault network. Here, we assess the relationship between fault complexity and slip segmentation in our preferred slip model using this metric.

Comparison of the preferred slip model with historical seismic ruptures and the fault misalignment results shows that slip terminations correspond closely to regions of high fault misalignment (Fig. 4). For example, the main slip area of segment F1 near the epicenter largely coincides with the 1956 M7.1 rupture, whereas its northern termination aligns with the 2012 M6.8 rupture. This area exhibits pronounced structural complexity, including splay faults and stepover structures with high fault misalignment. Near the southern termination of F1, abrupt changes in river course indicate substantial local terrain adjustments (Figs. 4 *A* and *C* and 5). Slip southward to ~21.5° latitude is markedly reduced; although R_M is lower here, GNSS data indicate that this segment was creeping at ~2.3 mm/y (25). Further south, slip resumes continuously to ~21° latitude, but is again interrupted by splay faults with high fault misalignment. South of the CCTV site, slip continues to the site of station NPW, where fault bending and splay faults coincide with high fault misalignment. The rupture extends through this complex structural zone, traversing the 1929 and 1930 rupture zones, and gradually diminishes and terminates.

Antoine et al. (18) inferred a relatively uniform slip model using geodetic observations, consistent with other geodetic-only models [(20, 22, 29); *SI Appendix*, Fig. S1], and discussed the relatively simple geometry of the central Sagaing fault in the context of fault maturity. In contrast, our joint inversion of teleseismic, geodetic, and near-fault strong-motion data reveals slip distribution with local segmentation. The boundaries of multiple slip segments in our preferred slip model generally correspond to regions of high fault misalignment, indicating structure-mediated rupture segmentation. Nevertheless, compared with more strongly segmented strike-slip earthquakes, such as the 2021 Maduo, Qinghai M7.3 earthquake (33) and the 2023 Turkey M7.8 mainshock (9), the surface rupture of the 2025 Myanmar earthquake is overall relatively continuous over a length of ~480 km, consistent with efficient rupture of a mature fault system (29), however localized deformation segmentation is observed at small scales along strike. Moreover, although shallow slip shows a spatial correlation with fault misalignment, it remains uncertain whether similar segmentation exists at depth based solely on surface fault trace data (51). Our model indicates that the overall rupture was dominated by continuous propagation, but was affected by local fault complexity, prior earthquake rupture zones and a creeping section, with resulting local-scale slip segmentation. Here we emphasize that local fault complexities, such as the splay faults and stepovers, are interpreted as potential structural controls on rupture behavior rather than from directly resolved rupture on secondary faults.

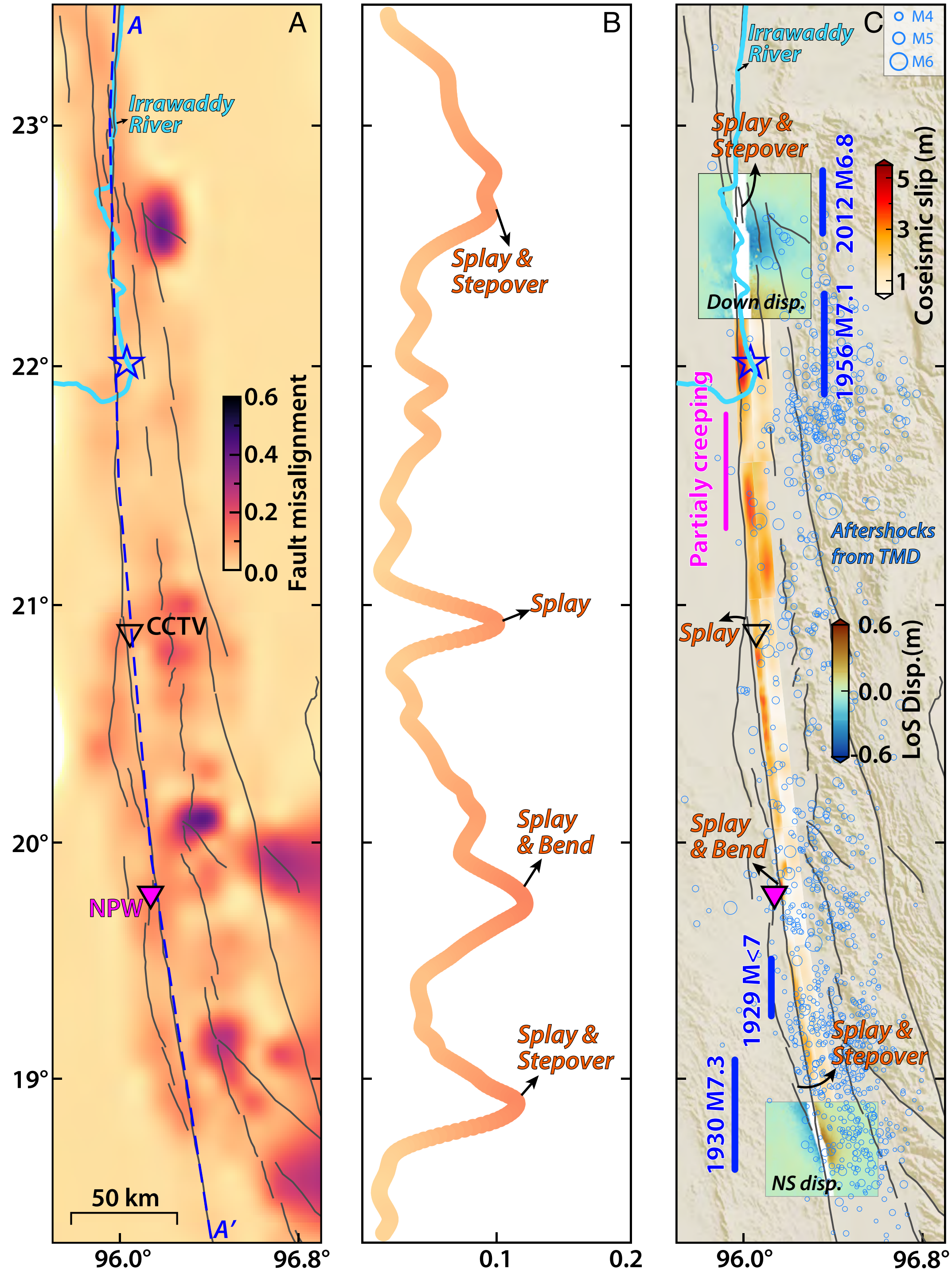

Fig. 4. (*A*) Fault misalignment along the Sagaing fault. Blue dashed line marks profile AA' shown in (*B*), and gray lines indicate regional faults from Zelenin et al. (50). (*B*) Fault misalignment profile along line AA', showing multiple local fault complex geometries with high fault misalignment exceeding 0.1. (*C*) Map view of the preferred slip model for the 2025 Myanmar earthquake. Solid blue line shows the lateral extent of historical ruptures, shifted in longitude for display; magenta line indicates interseismic creep section (25). The cyan curve represents the Irrawaddy River, blue star marks the epicenter of the 2025 Myanmar earthquake, and inverted triangles mark the CCTV and station NPW locations. Inset ALOS-2 LoS displacement fields highlight the different rupture termination patterns at the northern and southern ends. Light-blue circles show aftershocks from the Thai Meteorological Department catalog (TMD) for the 3 mo following the mainshock.

North–South Asymmetry in Local Rupture Behaviors. The preferred slip model reveals significant north–south asymmetry in rupture characteristics, not only in rupture length but also manifested in three other aspects (Figs. 3 and 4). The first asymmetry is that the slip magnitude and rupture area in segment F1 are larger than those in the southern segments. Paleoseismic evidence (16) indicates that this area has experienced multiple large slip events over the past 1,000 y, with individual coseismic displacements of 4 to 5 m, comparable to that in the 2025 Myanmar rupture. These repeated large slips suggest that segment F1 has historically accommodated significant rupture and can accumulate sufficient stress to produce large-magnitude events. The stress drop on the shallow segment F1 is 6.3 MPa (Fig. 3*B*), reflecting large stress accumulation and prolonged slip. The second asymmetry is the contrast in slip duration along the fault, with long-duration slip on the northern segment and short-duration slip on the southern segments (Fig. 3 *D* and *E*). Fig. 3*E* further reveals a systematic north-to-south shortening of the average local source time function (STF), with the duration varying from ~13.7 s on F1 to ~3.1 s on F3, accompanied by a progressive transition toward pulse-like rupture behavior. This evolution is supported by the near-fault observations at the NPW and CCTV sites. The local slip duration on F4 appears longer, possibly due to the local fault properties just before the whole rupture stopped. However, its occurrence in the late stage of the rupture is not well resolved with large uncertainties in the inversion. Overall, the north–south asymmetry in STF durations may result from a lower rigidity in the northern rupture area [(52), *SI Appendix*, Fig. S19], where repeated large-magnitude earthquakes near the epicenter may have promoted damage accumulation and the development of a fault damage zone (16, 53). Another possible explanation is that on a very long and narrow continental strike-slip fault, ruptures start with a crack-like source time function with long duration and evolve into a pulse-like rupture with shorter duration once the rupture distance exceeds the fault width (54). We also tested the southward-shifted epicenter estimated by Wei et al. [(25), *SI Appendix*, Fig. S20], which yields a slip distribution similar to the preferred model with no significant improvement in data fit. Such a shift would influence resolving local rise times, but the overall variation in STF durations among F1-F4 still holds. The third asymmetry is the contrasting rupture termination along the fault. In the north, rupture was abruptly halted by the fault's complex structure and by the stress shadow associated with the 2012 M6.8 earthquake, with an extensional stress regime producing the observed subsidence. In contrast, the more steeply dipping southern segment exhibits smooth, predominantly north–south displacement, indicating that local structural complexities and stress conditions control the rupture terminations.

Episodic Supershear–Subshear–Supershear Ruptures. The exceptionally long rupture length of the 2025 Myanmar earthquake provides an opportunity to evaluate whether the rupture became supershear and how long the supershear rupture, if it existed, was sustained. The spatiotemporal evolution of slip rate pattern in the preferred model (Fig. 5) reveals a clear intermittent supershear rupture behavior, characterized by alternating phases of acceleration and deceleration. Northward rupture propagation shows subshear speed of ~3.0 km/s and then rapidly terminates in the stress shadow region of the 2012 M6.8 earthquake, consistent with the unusual stopping behavior at the northern end discussed previously. Southward rupture also initiates at subshear speeds of 3.0 km/s and then undergoes a rapid deceleration at ~5 s after the origin time, coinciding with a creeping segment (25) and pronounced topographic variations in this region (5). The rupture accelerates and propagates southward at supershear speed until reaching the CCTV site, where it decelerates, with fault branching present. The local rupture speed at CCTV is ~3.4 km/s, calculated from the ~48 km distance between the preceding major slip patch at -76 km, where the slip exceeds 3 m, and the CCTV site at -124 km over a travel time of ~14 s. This slightly subshear speed is consistent with results reported by Hirano et al. (17) and Latour et al. (27). South of the CCTV site, the rupture accelerates again and propagates at supershear speeds toward station NPW, possibly involving in *P*-wave

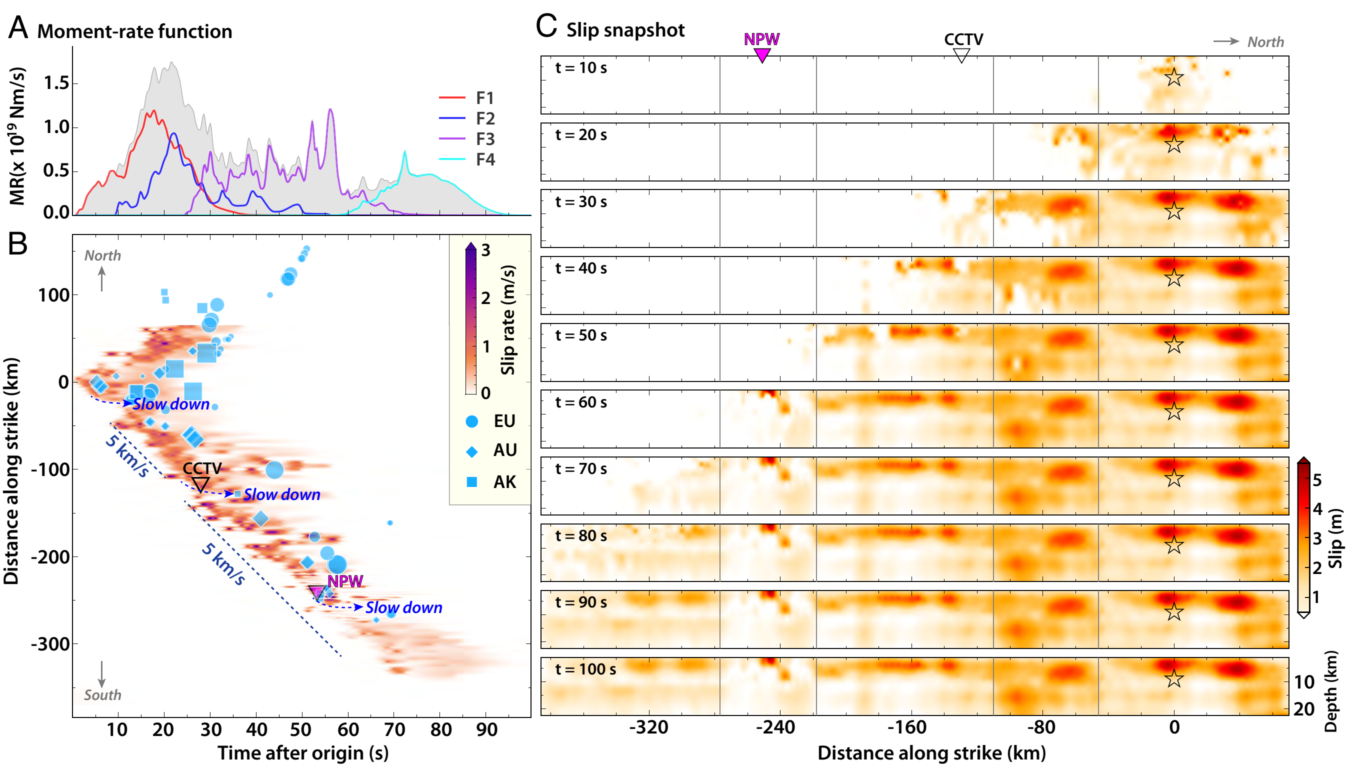

Fig. 5. (*A*) Far-field moment-rate function (MRF) for the whole rupture (gray). Color curves represent the energy release processes of each fault segment. (*B*) Temporal evolution of slip rate along the fault strike. The cyan polygons indicate the backprojection imaging results based on different seismic arrays (14). The colored background shows the variation of the average slip rate along strike, along with referenced rupture speeds. (*C*) Snapshots of cumulative slip distribution for 10-s intervals. Black outlined and magenta inverted triangles indicate the CCTV and station NPW locations, respectively.

triggering supershear rupture or acceleration toward P-wave speed. The local rupture speed at NPW is estimated to be ~5.5 km/s, calculated from the ~60 km distance between the preceding large slip patch at -180 km and station NPW at -240 km over a travel time of ~11 s. South of NPW, the rupture slowed down in a region of fault branching and bending, characterized by locally compressive stress on the Sagaing fault (5).

Sensitivity tests using different reference rupture speeds (3 to 6 km/s; *SI Appendix*, Figs. S21 and S22) show that the rupture propagation consistently exhibits localized deceleration near

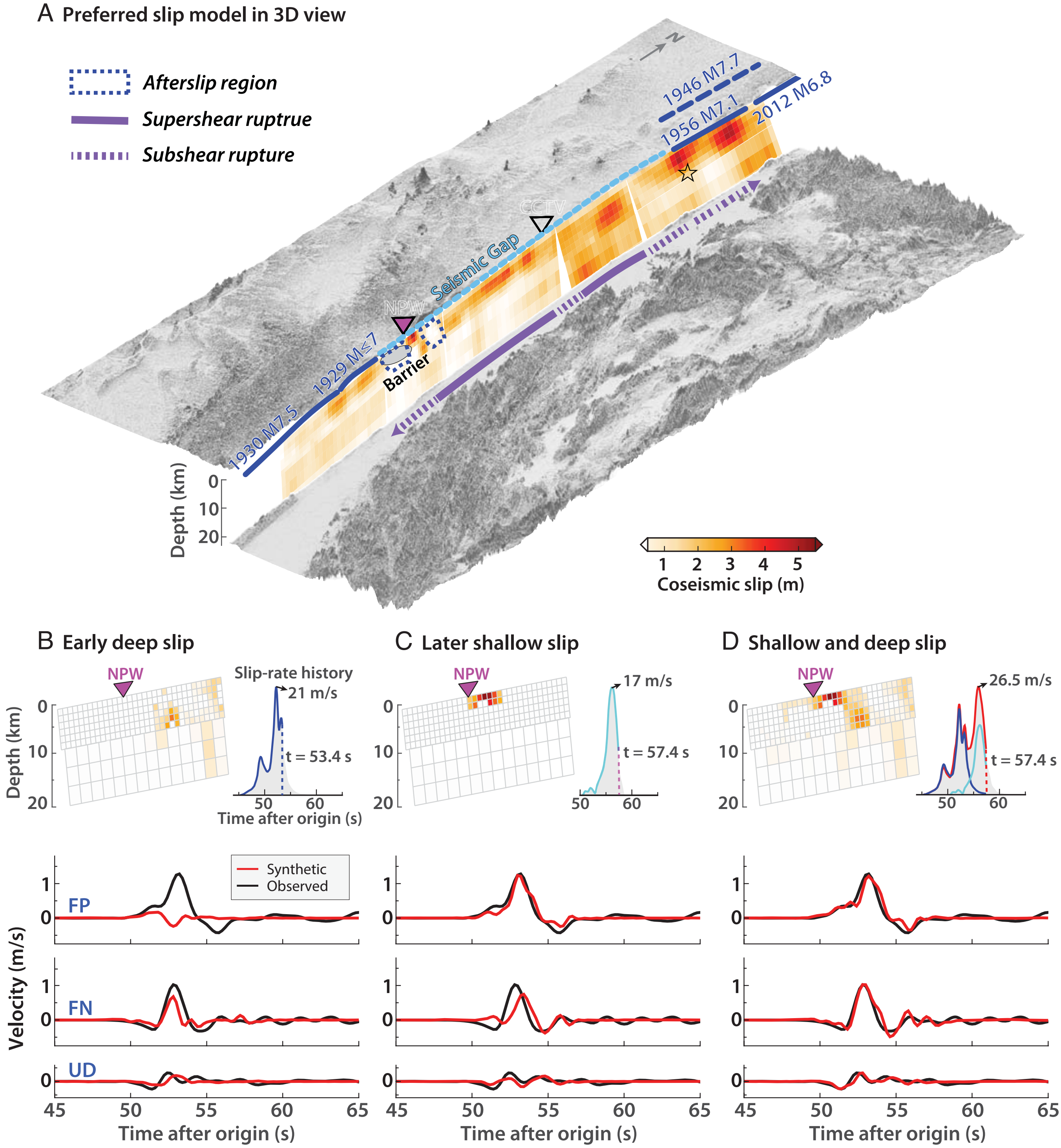

Fig. 6. (*A*) Preferred slip model in three-dimensional view with a step offset along the fault trace. Solid blue lines indicate the rupture extents of past events, and the dashed blue line marks the southern portion of the 1946 M7.7 rupture. Cyan line shows the seismic gap segment. Black star indicates the hypocenter. Purple solid and dashed lines represent the extents of supershear and subshear ruptures, respectively. Gray ellipse indicates the barrier located south of station NPW. Blue dashed rectangle outlines the afterslip region reported by Qiao et al. (20). (*B*–*D*) show the contributions of early deep slip, later shallow slip, and the combined deep and shallow slip to the waveform fitting at station NPW, respectively. *Inset* gray polygons show the far-field slip-rate function obtained by summing the slip-rate histories of the corresponding subfaults. Dashed lines indicate the end of the selected slip time windows with the slip models showing cumulative slip to the corresponding cut-off times (rupture expanded from *Right* to *Left* in these views from the east-southeast). Red and black lines in the ground velocity time series represent the synthetic and observed waveforms, respectively.

regions of slip segmentation. The pattern of rupture speed in the southern segment remains consistent across different reference rupture speeds, and no clear supershear rupture is resolved in the northern segment. In addition, regions with slip exceeding 3 m of segment F1 do not show rupture times earlier than those predicted by the local shear wave velocity (*SI Appendix*, Fig. S23), suggesting subshear rupture at the initial rupture stage. The resolution test on the local rupture speed (*SI Appendix*, Figs. S24–S26) further shows that the supershear–subshear–supershear pattern prescribed in the input model in the southern segment can be well recovered, while sustained supershear and depth-partitioned rupture scenarios would not reproduce a similar intermittent rupture pattern.

This sequence of supershear–subshear–supershear rupture pattern suggests that the supershear rupture did not propagate smoothly along the fault, but instead experienced intermittent modulation associated with local stress heterogeneity and structural complexity along the strike (Figs. 5 and 6). The episodic supershear behavior is reflected in the segmentation of the preferred slip model (Figs. 3 and 4), with lower slip during subshear phases and higher slip during supershear. Similar slip patterns have been reported in previous studies (13, 14), but our preferred slip model achieves higher resolution by using multiple data constraints and adaptive grid sizes. Such intermittent supershear behavior has also been observed in laboratory earthquake experiments, where rupture speed alternates in response to stress heterogeneities (34). The observed slip variations may reflect heterogeneous stress conditions along the fault, where locally higher stress levels may promote larger slip and rupture speed alternates in response to stress heterogeneities. Taken together, long-term stress accumulation on multiple asperities along the central Sagaing fault, coupled with amplification by free surface effects, can produce sufficiently large local energy releases to drive multiple episodes of intermittent stable supershear rupture without a transition distance (31, 34, 37). During the southward supershear rupture, a bimaterial effect may also play a role. The Shan Plateau on the eastern side of the Sagaing fault consists of harder metamorphic rocks compared with the softer sedimentary basin to the west (Fig. 1*B*). The rupture propagates in the direction of slip along the stiffer side, creating favorable conditions for supershear rupture (35, 36). Similar bimaterial contrasts have been discussed for other major strike-slip faults, such as the Hayward and San Andreas faults, but our source crustal velocity models are not well enough resolved to incorporate bimaterial structures in the inversion. In summary, the intermittent supershear rupture behavior revealed by our preferred slip model highlights the importance of local structural and stress variations along the Sagaing fault in mediating rupture dynamics during the 2025 Myanmar earthquake.

Dynamic Rupture Feature at Near-Fault Station NPW. The NPW strong-motion station, located only ~2.6 km from the fault, provides critical near-fault constraints on the local rupture history. The recorded ground velocity waveforms were rotated into fault-parallel (FP) and fault-normal (FN) components (Fig. 6 and *SI Appendix*, Fig. S17). The FP component shows a large positive pulse (~1.3 m/s) during the main-pulse stage, followed by a smaller reverse-polarity pulse, indicating changes in slip direction. Owing to the small grid size of the F3b subfault (1.8 × 1.5 km^2), the preferred model reproduces both the phase and amplitude of these pulses well. Tests with larger grid sizes degrade the waveform fit, highlighting the importance of fine fault discretization for resolving near-fault rupture features (*SI Appendix*, Fig. S27).

The main-pulse phase of the fault-parallel (FP) waveform requires a local rupture velocity exceeding $\sqrt{2}C_s$ (C_s: S-wave speed), while the smaller reverse-polarity pulse indicates a rupture stopping phase at a fault barrier (28). Forward modeling for our slip model yields an FP-to-FN amplitude ratio greater than 1, indicating a stable rupture speed above $\sqrt{2}C_s$ (55). This interpretation depends on the characteristic jump in waveform components rather than on their absolute amplitudes (56). The rupture speed of ~5.5 km/s near NPW further confirms the high local supershear rupture. The secondary pulse associated with rupture arrest corresponds to a slip gap between subfaults F3b and F4 south of NPW (Fig. 6*A*). This gap coincides with subtle deformation discontinuities in geodetic displacement fields evident in fault-parallel profiles, which show a reduction in deformation over a ~30 km zone south of NPW (*SI Appendix*, Fig. S28), consistent with the barrier location inferred by Ding et al. (28). Our preferred slip model indicates a barrier width of ~30 km, supporting their inference of a limited-scale barrier. Early postseismic study (20) further revealed up to ~2 m of shallow afterslip within ~20 to 30 km of both the northern and southern regions adjacent to NPW, consistent with the ~30 km spatial extent of the barrier (Fig. 6*A*). In addition to reproducing the main- and secondary-pulse of the FP component, our model also successfully fits the fault-normal (FN) and vertical (UD) waveforms, which were not well matched in previous dynamic simulations by Ding et al. (28). Separating deep and shallow slip contributions reveals that fitting the FN, FP, and UD components requires two distinct rupture processes (Fig. 6 *B–D*). The deep rupture arrives ~4 s earlier than the shallow rupture, with speed of ~5.5 km/s and ~4.8 km/s, respectively, supporting the complex rupture process both along-strike and along-dip fault directions near the site of station NPW.

Conclusion

In summary, we obtain the detailed rupture process by jointly using geodetic and seismic data to characterize key features of the 2025 M_W 7.7 Myanmar earthquake, including slip segmentation, north–south rupture asymmetry, and intermittent supershear rupture. Slip segmentation is associated with the fault misalignment metric, with slip termination zones consistently located in regions of high misalignment, corresponding to stepovers, bends, and branching structures. Rupture primarily propagated at supershear speeds in the southern segment, but decelerated when encountering local structural complexities before reaccelerating, producing an intermittent supershear pattern. In the northern segment, rupture was overall subshear and abruptly terminated upon entering the region of branching faults and stress shadow associated with the 2012 M6.8 event, exhibiting localized subsidence under an extensional stress regime. North–south differences are also evident in local slip duration, with northern subfaults exhibiting longer slip durations while southern segments progressively shorten before the end, likely reflecting the lower rigidity near the epicenter and the rupture dynamics being mediated by fault edges in long, narrow continental strike-slip faults. Our results demonstrate that local fault geometry and stress heterogeneity might govern slip distribution and rupture speed variations, emphasizing the importance of high-resolution near-fault observations for resolving detailed rupture dynamics.

Materials and Methods

Geodetic Data Processing. We collect and process the Sentinel-1A C-band Synthetic Aperture Radar (SAR), ALOS-2 L-band SAR, and Sentinel-2 optical satellite images (*SI Appendix*, Tables S1 and S2) to derive the coseismic surface deformation fields from different observational directions.

For the ALOS-2 SAR images, with a radar wavelength of ~24 cm, the differential interferometry technique (D-InSAR) is applied using the open-source ISCE-2 software (https://github.com/isce-framework/isce2) to derive the LoS coseismic deformation field. The longer wavelength provides higher coherence in densely vegetated areas, enabling more reliable near-fault deformation measurements than Sentinel-1A SAR images. Processing steps included 1) geocoding and terrain correction using a 30 m Shuttle Radar Topography Mission [SRTM, (57) Digital Elevation Model (DEM)]; 2) multilooking size of 5 pixels × 28 pixels (range × azimuth) and adaptive filtering to improve signal-to-noise ratio (SNR); 3) ionospheric correction with multilooking size of 1 pixel × 14 pixels to improve phase SNR (58); 4) phase unwrapping with SNAPHU algorithm (59); 5) geocoding of the unwrapped phase; and 6) residual long-wavelength phase removal by polynomial fitting.

For the Sentinel-2 optical images, we apply the subpixel cross-correlation method to derive the coseismic surface deformation field at 10 m spatial resolution using the MicMac software (https://github.com/micmacIGN/micmac). The pre- and postseismic images are correlated with a sliding window of 3 pixels × 3 pixels and a regularization coefficient of 0.3 was adopted for the correlation. The preliminary deformation field is further processed with coherence masking, destriping, detrend correction, and nonlocal means filtering (60) to improve SNR (*SI Appendix*, Fig. S29). We apply a distance-weighted downsample method to reduce the ALOS-2 SAR and Sentinel-2 optical deformation fields for subsequent joint inversion, with each dataset containing 1,500 to 2,000 points.

For the Sentinel-1A SAR images, we directly download the azimuth displacement field data from Wang and Xu (61), which were processed using the pixel offset tracking (POT) method. This approach estimates surface displacement in the azimuth direction through cross-correlation of Single Look Complex (SLC) SAR images with a search window of 64 pixels × 64 pixels (range × azimuth). For large earthquakes, POT method can provide more reliable near-fault deformation measurements compared with D-InSAR techniques.

Seismic Data Processing. We use teleseismic data with good azimuthal coverage, with a maximum azimuthal gap of 36°, to constrain the rupture process. The teleseismic dataset includes 64 teleseismic *P* displacements and 35 *SH* velocity filtered in the frequency band 0.005 to 0.9 Hz. The spatial distribution of the teleseismic stations is shown in *SI Appendix*, Fig. S3. Additionally, long-period teleseismic surface waves are incorporated to further stabilize the seismic moment in the inversion, including 23 Rayleigh and 22 Love waves from IRIS-DMC. The station distribution is shown in *SI Appendix*, Fig. S4, and a passband filter of 0.004 to 0.006 Hz is applied.

We collect and process a total of five near-fault strong-motion stations to constrain the rupture process, ranked by epicentral distance as MM.NGU, GE.NPW, MM.KTN, IU.CHTO, and MM.YGN, with station locations shown in *SI Appendix*, Fig. S5. NPW is particularly close to the fault, located only 2.6 km away, and its records exhibit baseline offsets due to intense surface deformation. Baseline corrections are applied (14), yielding results consistent with those of Lai et al. (62) and Ye et al. (14), effectively capturing the coseismic displacement evolution at NPW, with a final static displacement of ~1.6 m. After baseline correction, the velocity records are low-pass filtered below 0.5 Hz for finite-fault inversion. Because stations CHTO, YGN, and KTN exceed 300 km distance and the terrain around stations CHTO and KTN is complex, uncertainties in the velocity structure pose challenges to model these strong-motion waveforms. Therefore, we exclude these three stations from the inversion and use only the NPW and NGU records, which are closer to the fault.

Finite-Fault Inversion. We adapt a nonlinear finite-fault inversion method (63, 64) to support variable fault grid sizes in both strike and dip directions. We obtain the detailed rupture process, including slip amplitude, slip rate, rake angle, source time function, and rupture speed of each subfault, with this nonlinear joint inversion of seismic and static geodetic data. The objective function in the inversion is defined as $e_{wf} + W_{static} \bullet e_{static} + W_s \bullet S + W_M \bullet M + W_T \bullet T$, where the e_{wf} is the waveform misfit, e_{static} is the static data misfit, S is the spatial smoothing operator, M is the given normalized seismic moment for moment constraint, T is the time smoothing operator, W_{static}, W_s, W_M, and W_T are the relative weighting for static misfit, spatial smoothing, seismic moment constraint, and time smoothing, respectively. The waveform misfit is calculated using the combined L1 and L2 norms of wavelet-domain waveforms. The static data misfit is calculated using the sum of squared residuals.

Based on fault traces derived from geodetic observations (Fig. 2), we divide the seismic fault from north to south into four segments (F1 to F4) and determine their strikes at 358°, 356°, 354°, and 350°, respectively. The fault is further divided into deep and shallow sections at a depth of 10 km, with deep grids of 4.0 × 5.0 km^2 (strike × dip) for all segments. The shallow grids vary to account for near-fault data: F1, F2, and F4 have 4.0 × 2.0 km^2 grids, F3 is subdivided into F3a (4.0 × 2.0 km^2) and F3b (1.8 × 1.5 km^2) near station NPW. Considering the observed increase of dip from north to south, we set the dips of F1 to F4 at 50°, 60°, 80°, and 85°, respectively, all with eastward dipping direction. Rake angles are constrained to capture minor vertical slip, with 170° to 190° for F2 and 160° to 200° for the other segments (*SI Appendix*, Fig. S30 and Table S3).

We set the considered slip range of each subfault to 0 to 7 m and represent the source time function of each subfault using an asymmetric cosine function. The allowed duration of each subfault is in the range 1.2 to 28.8 s with a time step of 0.6 s to accommodate shorter slip durations. Rupture speed is constrained based on the NPW waveform time records and backprojection results (14), with a reference average speed of 5 km/s and allowed range of variation of 2 to 8 km/s for each segment. Detailed parameters are listed in *SI Appendix*, Table S3. Green's functions for strong-motion and static data are computed using the F-K method (65) with a one-dimensional regional velocity model [(66), *SI Appendix*, Fig. S31]. We assign different weights to teleseismic body waves, long-period surface waves, near-fault strong-motion data, SAR, and optical observations according to data quality and spatiotemporal resolution to optimally utilize multisource data in the inversion (*SI Appendix*, Table S4).

Fault Misalignment Calculation. We quantitatively characterize the structural complexity of the fault system using the fault misalignment R_M (49) to evaluate variations in fault strike orientations. When faults exhibit a dominant strike direction, the difference between the maximum and minimum projected lengths is large, indicating low fault misalignment. For parallel faults, $R_M = 0$, and the value increases with greater strike variability. Regional fault data are obtained from the Active Faults of Eurasia Database [AFEAD; (50)], which provides detailed mapping faults in Myanmar at a scale of 1:1,000,000. The study area is divided into regular grids to calculate R_M, and three grid sizes (0.1°, 0.2°, and 0.3°) are tested, as shown in *SI Appendix*, Fig. S32. Considering both spatial resolution and consistency with surface fault traces, a grid size of 0.2° is selected for analysis (Fig. 4*A*).

Data, Materials, and Software Availability. All datasets used in this study for joint inversion are available on Zenodo (https://zenodo.org/records/18352884). The processed Sentinel-1A SAR data are available in Wang and Xu (61) (https://zenodo.org/records/15465249). The open-source MicMac software can be downloaded from https://github.com/micmacIGN/micmac, and the open-source ISCE-2 code is publicly available at https://github.com/isce-framework/isce2.

ACKNOWLEDGMENTS. We thank Prof. Shiqing Xu, Prof. Ahmed Elbanna, two anonymous reviewers, and the editor John Vidale for constructive discussion and comments, which have helped improve our manuscript. We thank Xiaohua Xu and Xin Wang from University of Science and Technology of China for providing the processed Sentinel-1A SAR data, Bo Li and Xin Qiao for sharing their respective slip models. The work was supported in part by National Natural Science Foundation of China (42474077, 42274075) and National Science Foundation Grant EAR1802364 (T.L.).

Author affiliations: [a]Department of Earth and Space Sciences, Southern University of Science and Technology, Shenzhen 518055, China; [b]State Key Laboratory of Earth and Planetary Physics, Institute of Geology and Geophysics, Chinese Academy of Sciences, Beijing 100029, China; and [c]Department of Earth and Planetary Sciences, University of California Santa Cruz, Santa Cruz, CA 95064

Author contributions: L.Y. designed research; T.X. and L.Y. performed research; J.H., H.G., and Z.Y. contributed new reagents/analytic tools; T.X., L.Y., J.H., and X.D. analyzed data; and T.X., L.Y., and T.L. wrote the paper.

1. R. Mallick *et al.*, Active convergence of the India-Burma-Sunda plates revealed by a new continuous GPS network. *J. Geophys. Res.* **124**, 3155–3171 (2019).
2. T. Z. H. Tin *et al.*, Present-day crustal deformation and slip rate along the southern Sagaing fault in Myanmar by GNSS observation. *J. Asian Earth Sci.* **228**, 105125 (2022).
3. W. Fadil *et al.*, Active faults revealed and new constraints on their seismogenic depth from a high-resolution regional focal mechanism catalog in Myanmar (2016–2021). *Bull. Seismol. Soc. Am.* **113**, 613–635 (2023).
4. Y. Wang *et al.*, Active tectonics and earthquake potential of the Myanmar region. *J. Geophys. Res.: Solid Earth* **119**, 3767–3822 (2014).
5. S. T. Tun, I. M. Watkinson, "Chapter 19: The Sagaing fault, Myanmar" in *Myanmar: Geology, Resources and Tectonics*, A. J. Barber, K. Zaw, M. J. Crow, Eds. (London Geological Society, 2017). pp. 413-441.
6. N. Hurukawa, P. Maung Maung, Two seismic gaps on the Sagaing Fault, Myanmar, derived from relocation of historical earthquakes since 1918. *Geophys. Res. Lett.* **38**, 1 (2011).
7. M. Abdelmeguid *et al.*, Dynamics of episodic supershear in the 2023 M7.8 Kahramanmaraş/Pazarcik earthquake, revealed by near-field records and computational modeling. *Commun. Earth Environ.* **4**, 456 (2023).
8. X. Ding *et al.*, The sharp turn: Backward rupture branching during the 2023 M_W 7.8 Kahramanmaraş (Türkiye) earthquake. *Seismica* **2**, 3 (2023).
9. C. Ren *et al.*, Supershear triggering and cascading fault ruptures of the 2023 Kahramanmaraş, Türkiye, earthquake doublet. *Science* **383**, 305–311 (2024).
10. E. O. Lindsey *et al.*, Active subduction and strain partitioning in western Myanmar revealed by a dense survey GNSS network. *Earth Planet. Sci. Lett.* **622**, 118384 (2023).
11. United States Geological Survey, M7.7-2025 Mandalay, Burma (Myanmar) Earthquake, (2025), https://earthquake.usgs.gov/earthquakes/eventpage/us7000pn9s/executive.
12. Democratic Voice of Burma, Death Toll from Myanmar's Earthquake Reaches, (2025), https://burmese.dvb.no/live.
13. N. Inoue *et al.*, A multiple asymmetric bilateral rupture sequence derived from the peculiar teleseismic P-waves of the 2025 Mandalay, Myanmar earthquake. *Seismica* **4**, 1 (2025).
14. L. Ye, T. Lay, H. Kanamori, The 28 March 2025 MW 7.8 Myanmar earthquake: Preliminary analysis of an ~480 km long intermittent supershear rupture. *The Seismic Record* **5**, 260-269 (2025).
15. Z. Peng *et al.*, Mainshock rupture properties, aftershock activities and remotely triggered seismicity associated with the 2025 MW 7.7 Sagaing fault earthquake in Myanmar. *Earthq. Res. Adv.* **5**, 100413 (2025).
16. D. Melgar *et al.*, Supershear source model of the 2025 M_W 7.8 Myanmar earthquake and paleoseismology of the Sagaing Fault: Regions of significant overlap with past earthquakes. *Seismica* **4**, 2 (2025).
17. S. Hirano, R. Doke, T. Maeda, Supershear-subshear-supershear rupture sequence during the 2025 Mandalay earthquake in Myanmar. *Seismica* **4**, 2 (2025).
18. S. L. Antoine *et al.*, The 2025 M_W 7.7 Mandalay, Myanmar, earthquake reveals a complex earthquake cycle with clustering and variable segmentation on the Sagaing Fault. *Proc. Natl. Acad. Sci. U.S.A.* **122**, e2514378122 (2025).
19. F. Vera *et al.*, Supershear rupture along the Sagaing fault seismic gap: The 2025 Myanmar earthquake. *Seismic Record* **5**, 289–299 (2025).
20. X. Qiao *et al.*, Coseismic slip and early rapid afterslip of the 2025 M_W 7.7 Myanmar earthquake constrained by space-based geodetic observations. *Geophys. Res. Lett.* **52**, e2025GL118226 (2025).
21. B. Li *et al.*, Seismic gap breached by the 2025 M_W 7.7 Mandalay (Myanmar) earthquake. *Nat. Geosci.* **18**, 1–9 (2025).
22. Y. Li *et al.*, Sustained supershear rupture during the 2025 Mandalay. Myanmar earthquake. *Commun. Earth Environ.* **6**, 1030 (2025).
23. Q. Yao, C. Yu, M. Zhou, Bilateral supershear rupture of the 2025 M_W 7.7 Myanmar earthquake imaged by global P-wave and regional surface-wave back-projections. *Geophys. Res. Lett.* **52**, e2025GL116800 (2025).
24. D. E. Goldberg *et al.*, Ultralong, supershear rupture of the 2025 M_W 7.7 Mandalay earthquake reveals unaccounted risk. *Science* **390**, 458–462 (2025).
25. S. Wei *et al.*, Supershear rupture sustained through a thick fault zone in the 2025 M_W 7.8 Mandalay earthquake. *Science* **390**, 468–475 (2025).
26. L. Xu *et al.*, Bimaterial effect and favorable energy ratio enabled supershear rupture in the 2025 Mandalay earthquake. *Science* **390**, 476–481 (2025).
27. S. Latour *et al.*, Direct estimation of earthquake source properties from a single CCTV camera. *Science* **390**, 463–467 (2025).
28. X. Ding, S. Xu, L. Ye, Intermittent supershear rupture punctuated by barrier-induced stopping phase during the 2025 M_W 7.8 Myanmar earthquake: Evidence from near-fault strong motion observation. *Geophys. Res. Lett.* **52**, e2025GL118863 (2025).
29. E. O. Lindsey *et al.*, Mature fault mechanics revealed by the highly efficient 2025 Mandalay earthquake. *Nat. Commun.* **16**, 10937 (2025).
30. S. L. Antoine *et al.*, Diffuse deformation and surface faulting distribution from submetric image correlation along the 2019 Ridgecrest, California, ruptures. *Bull. Seismol. Soc. Am.* **111**, 2275–2302 (2021).
31. L. Bruhat, Z. Fang, E. M. Dunham, Rupture complexity and the supershear transition on rough faults. *J. Geophys. Res.: Solid Earth* **121**, 210–224 (2016).
32. Y. Liu, N. Lapusta, Transition of mode II cracks from sub-Rayleigh to intersonic speeds in the presence of favorable heterogeneity. *J. Mech. Phys. Solids* **56**, 25–50 (2008).
33. J. Liu-Zeng *et al.*, Fault orientation trumps fault maturity in controlling coseismic rupture characteristics of the 2021 Maduo earthquake. *AGU Adv.* **5**, 2 (2024).
34. S. Xu *et al.*, Fault strength and rupture process controlled by fault surface topography. *Nat. Geosci.* **16**, 94–100 (2023).
35. Y. Ben-Zion, Recent results on dynamic rupture in earthquake fault models. *J. Mech. Phys. Solids* **49**, 2209–2244 (2001).
36. Y. Ben-Zion, C. G. Sammis, Characterization of fault zones. *Pure Appl. Geophys.* **160**, 677–715 (2003).
37. Y. Kaneko, N. Lapusta, Supershear transition due to a free surface in 3-D simulations of spontaneous dynamic rupture on vertical strike-slip faults. *Tectonophysics* **493**, 272–284 (2010).
38. M. Bouchon *et al.*, Faulting characteristics of supershear earthquakes. *Tectonophysics* **493**, 244–253 (2010).
39. K. Xia, A. J. Rosakis, H. Kanamori, J. R. Rice, Laboratory earthquakes along inhomogeneous faults: Directionality and supershear. *Science* **308**, 681–684 (2005).
40. B. Delouis, M. van den Ende, J. P. Ampuero, Kinematic rupture model of the 6 February 2023 M_W 7.8 Türkiye earthquake from a large set of near-source strong-motion records combined with GNSS offsets reveals intermittent supershear rupture. *Bull. Seismol. Soc. Am.* **114**, 726–740 (2024).
41. United States Geological Survey, M 6.7-2025 Mandalay, Burma (Myanmar) Earthquake, (2025), https://earthquake.usgs.gov/earthquakes/eventpage/us7000pn9z/executive.
42. L. Ye, T. Lay, H. Kanamori, L. Rivera, Rupture characteristics of major and great (MW≥7.0) megathrust earthquakes from 1990 to 2015: 1. Source parameter scaling relationships. *J. Geophys. Res.: Solid Earth* **121**, 826–844 (2016).
43. Y. Okada, Internal deformation due to shear and tensile faults in a half-space. *Bull. Seismol. Soc. Am.* **82**, 1018–1040 (1992).
44. J. Kearse, Y. Kaneko, Curved fault slip captured by CCTV video during the 2025 MW 7.7 Myanmar earthquake. *Seismic Record* **5**, 281–288 (2025).
45. Z. Wan *et al.*, Along-strike variation of rupture characteristics and aftershock patterns of the 2023 M_W 7.8 türkiye earthquake controlled by fault structure. *Seismol. Res. Lett.* **95**, 2071–2080 (2024).
46. B. Wang, S. Barbot, Rupture segmentation on the east anatolian fault (Turkey) controlled by along-strike variations in long-term slip rates in a structurally complex fault system. *Geology* **52**, 779–783 (2024).
47. J. Lee *et al.*, Fault-network geometry influences earthquake frictional behaviour. *Nature* **631**, 106–110 (2024).
48. C. Perrin *et al.*, Location of largest earthquake slip and fast rupture controlled by along-strike change in fault structural maturity due to fault growth. *J. Geophys. Res.: Solid Earth* **121**, 3666–3685 (2016).
49. S. X. Chu, V. C. Tsai, D. T. Trugman, G. Hirth, Fault interactions enhance high-frequency earthquake radiation. *Geophys. Res. Lett.* **48**, 20 (2021).
50. E. Zelenin *et al.*, The Active Faults of Eurasia Database (AFEAD): The ontology and design behind the continental-scale dataset. *Earth Syst. Sci. Data.* **14**, 4489–4503 (2022).
51. J. F. Dolan, B. D. Haravitch, How well do surface slip measurements track slip at depth in large strike-slip earthquakes? The importance of fault structural maturity in controlling on-fault slip versus off-fault surface deformation *Earth Planet. Sci. Lett.* **388**, 38–47 (2014).
52. X. Wang *et al.*, A 3-D shear wave velocity model for Myanmar region. *J. Geophys. Res.: Solid Earth* **124**, 504–526 (2019).
53. Y. Huang, J. P. Ampuero, D. V. Helmberger, The potential for supershear earthquakes in damaged fault zones–theory and observations. *Earth Planet. Sci. Lett.* **433**, 109–115 (2016).
54. S. M. Day, Three-dimensional finite difference simulation of fault dynamics: Rectangular faults with fixed rupture velocity. *Bull. Seismol. Soc. Am.* **72**, 705–727 (1982).
55. M. Mello, H. S. Bhat, A. J. Rosakis, Spatiotemporal properties of Sub-Rayleigh and supershear rupture velocity fields: Theory and experiments. *J. Mech. Phys. Solids* **93**, 153–181 (2016).
56. A. Rosakis, M. Abdelmeguid, A.E. Elbanna, Near-field evidence for early supershear rupture of the M_W 7.8 Kahramanmaraş earthquake in Turkey. *Nat. Geosci.* **18**, 534–541 (2025).
57. T. G. Farr *et al.*, The shuttle radar topography mission. *Rev. Geophys.* **45**, 2 (2007).
58. C. Liang, E. J. Fielding, Interferometry with ALOS-2 full-aperture ScanSAR data. *IEEE Trans. Geosci. Remote Sens.* **55**, 2739–2750 (2017).
59. C. W. Chen, H. A. Zebker, Network approaches to two-dimensional phase unwrapping: Intractability and two new algorithms. *J. Opt. Soc. Am. A.* **17**, 401–414 (2000).
60. A. Buades, B. Coll, J. M. Morel, Nonlocal image and movie denoising. *Int. J. Comput. Vis.* **76**, 123–139 (2008).
61. X. Wang, X. Xu, Coseismic surface deformation of the 2025 Myanmar M_W 7.7 earthquake revealed by Sentinel-1 Pixel offset tracking and DInSAR analyses. Zenodo, https://zenodo.org/records/15465249 (2025).
62. S. T. Lai *et al.*, Capacity building enables unique near-fault observations of the destructive 2025 M_W 7.7 Myanmar earthquake. *Earth Syst. Sci. Data.* **17**, 5149–5164 (2025).
63. C. Ji, D. J. Wald, D. V. Helmberger, Source description of the 1999 Hector Mine, California, earthquake, part I: Wavelet domain inversion theory and resolution analysis. *Bull. Seismol. Soc. Am.* **92**, 1192–1207 (2002).
64. G. Shao, X. Li, C. Ji, T. Maeda, Focal mechanism and slip history of the 2011 M_W 9.1 off the Pacific coast of Tohoku earthquake, constrained with teleseismic body and surface waves. *Earth Planet. Sci.* **63**, 559–564 (2011).
65. L. Zhu, L. A. Rivera, A note on the dynamic and static displacements from a point source in multilayered media. *Geophys. J. Int.* **148**, 619–627 (2002).
66. H. A. Shiddiqi, P. P. Tun, L. Ottemöller, Minimum 1D velocity model and local magnitude scale for Myanmar. *Seismol. Res. Lett.* **90**, 1923–1936 (2019).

Supporting Information for

Asymmetric and Intermittent Supershear Rupture Mediated by Local Fault Complexity during the 2025 M_W 7.7 Myanmar Earthquake

Tao Xia[1], Lingling Ye[1,*], Jinlai Hao[2], Haijun Gao[1], Thorne Lay[3], Xiaotian Ding[1], Zhenxing Yao[2]

1. Department of Earth and Space Sciences, Southern University of Science and Technology, Shenzhen, China

2. State Key Laboratory of Earth and Planetary Physics, Institute of Geology and Geophysics, Chinese Academy of Sciences, Beijing, China

3. Department of Earth and Planetary Sciences, University of California Santa Cruz, Santa Cruz, California, U.S.A.

corresponding author: Lingling Ye
Email: yell@sustech.edu.cn

This PDF file includes:

Text S1
Figures S1 to S32
Tables S1 to S4

Text S1. Checkerboard and Sensitivity Tests

To evaluate the spatial resolution of the preferred slip model, we conduct two checkerboard tests with specified slip distributions used to compute predictions corresponding to all observed data, which are then jointly inverted for slip models.

The first input model (Model 1) is constructed to reflect the overall spatial characteristics of the preferred slip model. In this model, alternating slip patches with an amplitude of 4 m and rake of 175° are assigned across the fault plane. Each subfault is assigned a slip duration of 8.4 s, and rupture speed is prescribed with a constant value of 5 km/s. Synthetic datasets, including teleseismic waveforms, near-fault strong-motion records, long-period surface waveforms, and geodetic surface deformation, are forward generated at the observation locations. The inversion is then performed using the same data weighting setting and inversion parameters as in the real-data inversion. The result is shown in Figure S6.

The second input model (Model 2) consists of a regular checkerboard pattern with a uniform patch size of 12 km × 10 km (strike × dip). In this case, the slip amplitude is set to 6 m with a rake of 175°, while the slip duration (8.4 s) and rupture speed (5 km/s) are kept the same as in Model 1. Synthetic datasets are generated in the same manner and inverted using the identical inversion setup. The result is shown in Figure S7.

We also tested the southward-shifted epicenter estimated by Wei et al. (*1*), with all other inversion parameters identical to those of the preferred model. The inverted model has a slip distribution similar to the preferred model with no significant improvement in data fit. Such a shift but may influence rise-time asymmetry due to the effect of fault width (Fig. S20).

To evaluate the resolution of local rupture speed in our joint inversion, we present tests to evaluate whether the joint inversion can resolve variation in rupture speed along strike, including sensitivity tests using different reference rupture speeds in the inversion (Figs. S21-S23), a checkerboard resolution test (Fig. S24), and two synthetic tests based on sustained supershear model (5.0 km/s, Fig. S25) along with depth-partitioned rupture model (Fig. S26) with shallow subshear (2.5 km/s) and deep supershear (5.0 km/s) propagation. These tests demonstrate that the main supershear-subshear-supershear rupture along strike to the south can be recovered within the resolution of our inversion, while sustained supershear and depth-partitioned rupture scenarios do not reproduce similar intermittent rupture-speed variations, supporting the validity of our inferred intermittent supershear rupture interpretation. The reference rupture speed tests (Fig. S23) do not provide unambiguous evidence of supershear rupture in the northern segment or near the epicenter of the southern rupture. Accordingly, we have moderated our interpretation of supershear rupture in the early stage in both rupture directions to account for resolution limitations.

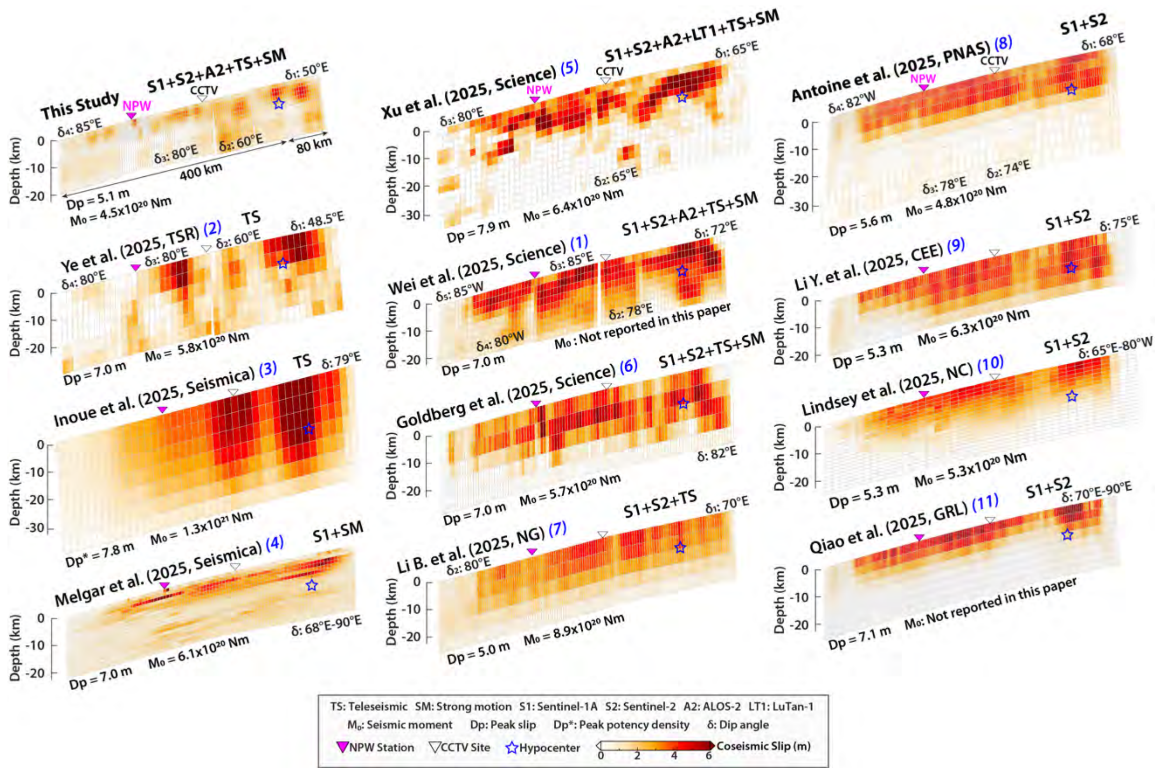

Figure S1. Comparison between our preferred slip model and previously published slip models (references and analyzed data types are indicated for each study). Faulting geometries are indicated along strike.

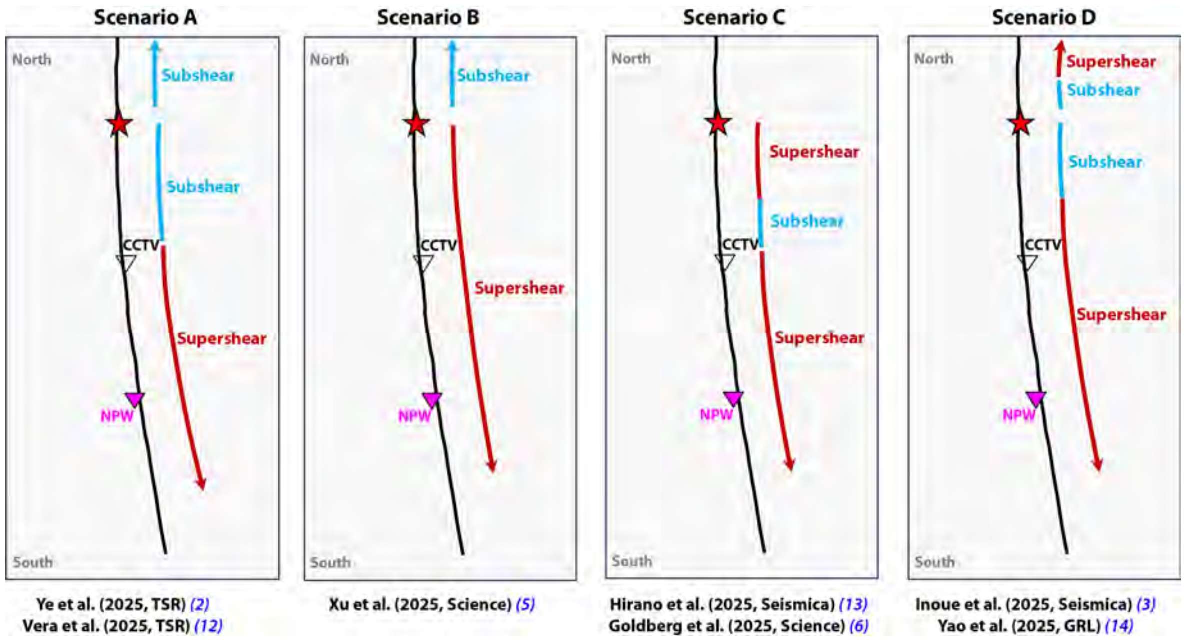

Figure S2. Summary map views of published interpretations of rupture-speed evolution for the 2025 Myanmar earthquake. Blue and red lines indicate regions of subshear and supershear rupture, respectively. Inverted triangles denote the locations of station NPW and the CCTV site. Red star indicates the epicenter.

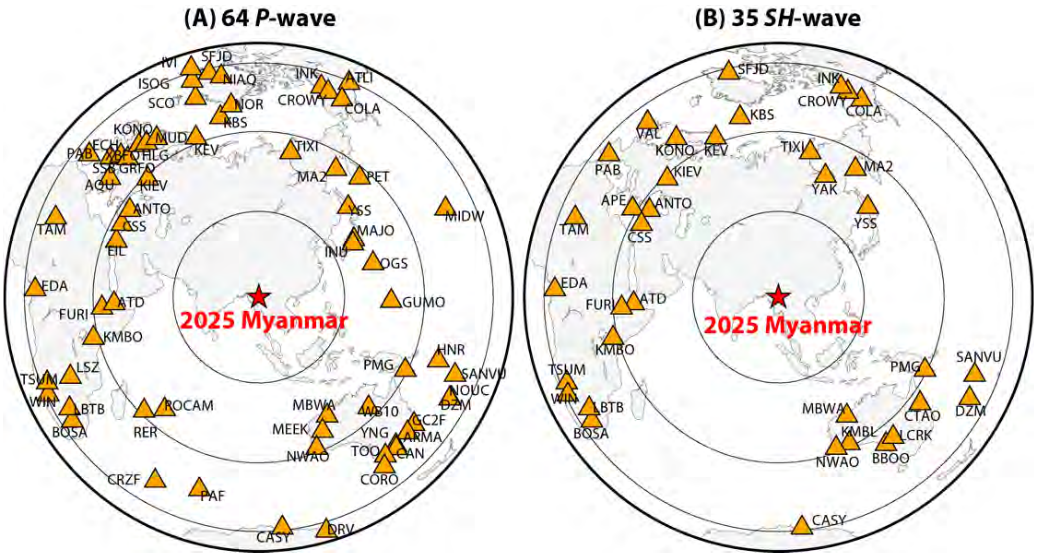

Figure S3. (A) Distribution of 64 teleseismic *P*-wave and (B) 35 teleseismic *SH*-wave stations used in this study. Orange triangles indicate station locations, labeled with the corresponding station names. Red star marks the epicenter of the 2025 Myanmar earthquake. Circles represent epicentral distances of 30°, 60°, and 90°.

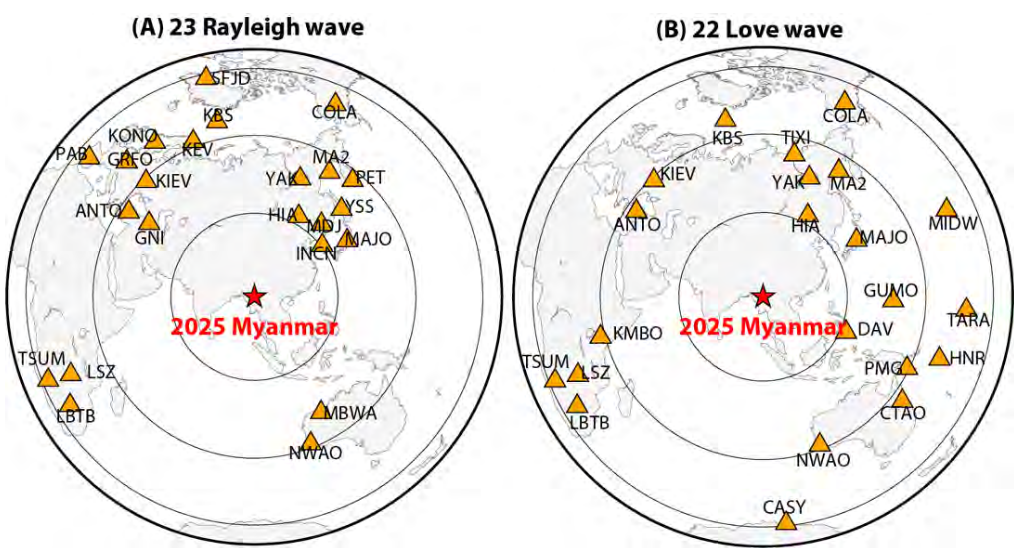

Figure S4. (A) Distribution of 23 long-period Rayleigh wave and (B) 22 Love wave recordings used in this study. Orange triangles indicate station locations, labeled with the corresponding station names. Red star marks the epicenter of the 2025 Myanmar earthquake. Circles represent epicentral distances of 30°, 60°, and 90°.

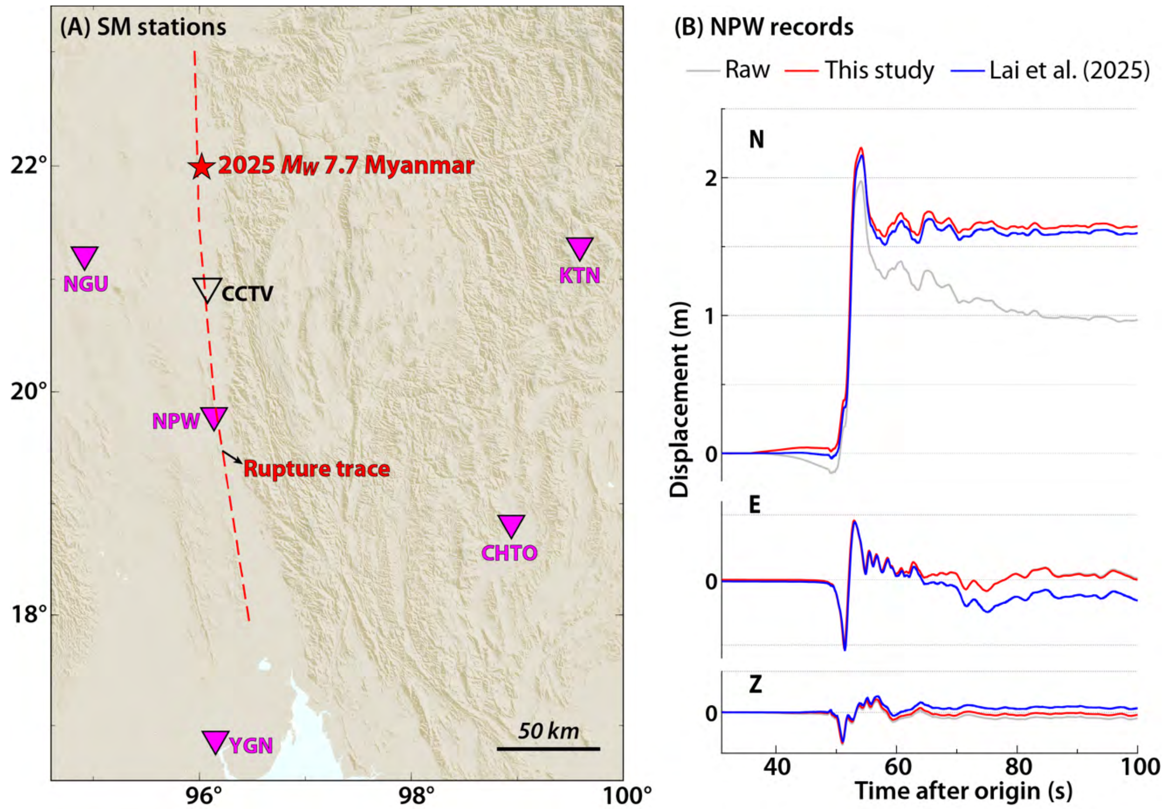

Figure S5. (A) Distribution of strong-motion stations considered in this study. Red dotted line indicates the surface rupture trace derived from geodetic observations. Magenta inverted triangles mark the strong-motion station locations. Red star marks the epicenter of the 2025 Myanmar earthquake, and black inverted triangle indicates the CCTV location capturing fault slip. NPW and NGU observations are incorporated in the joint inversions. (B) Comparison of the three-component displacement waveforms at the NPW station before and after baseline correction. Gray lines show the displacements obtained by double integration of the original acceleration waveform, red lines show the displacements after baseline correction applied in this study, and blue lines show the baseline-corrected displacements from Lai et al. (*15*). The vertical scales of the N, E, and Z components are the same.

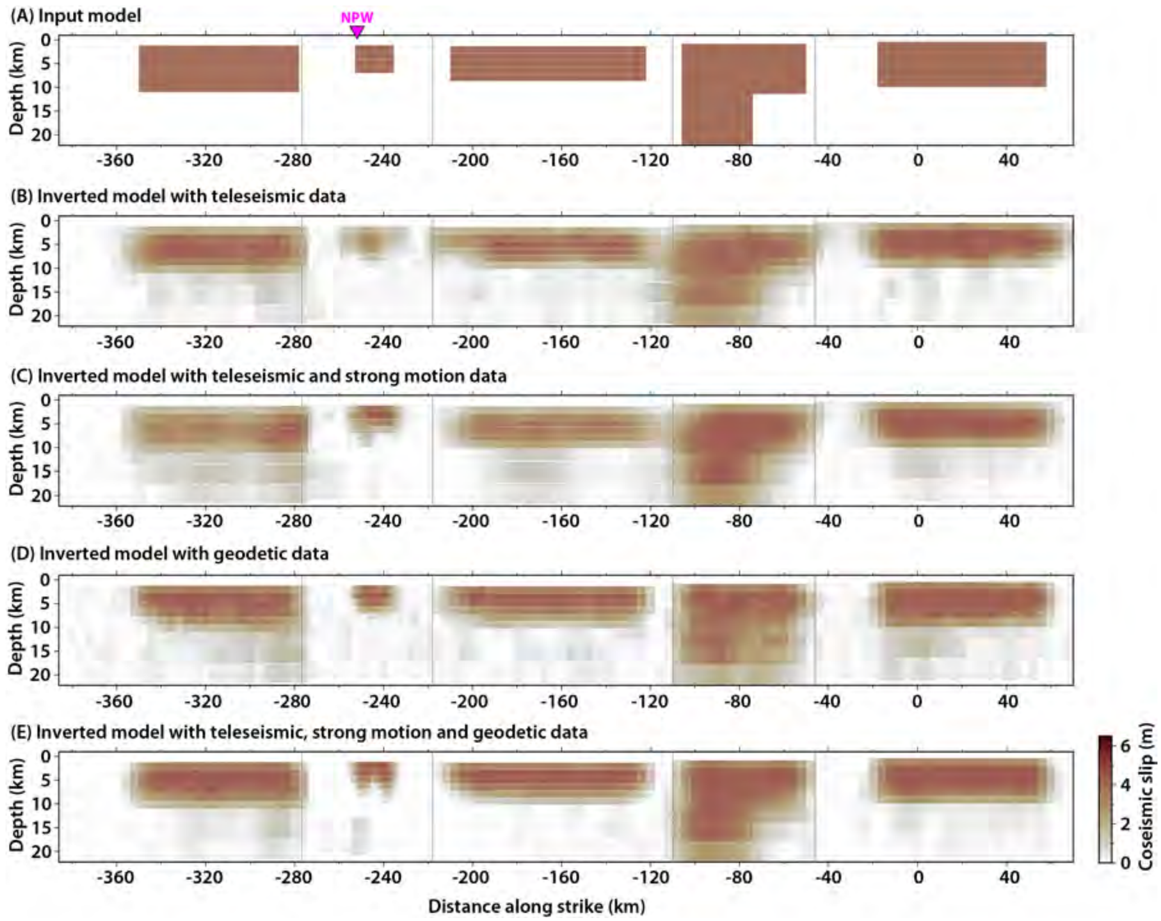

Figure S6. Checkerboard test applied to different synthetic datasets for an input slip distribution approximating the spatial pattern of the joint inversion result (Model 1). (A) Input model. (B) Inversion using teleseismic data. (C) Inversion using teleseismic and near-fault strong-motion data. (D) Inversion using geodetic data. (E) Inversion using teleseismic, near-fault strong-motion, and geodetic data. Magenta inverted triangle indicates the station NPW location.

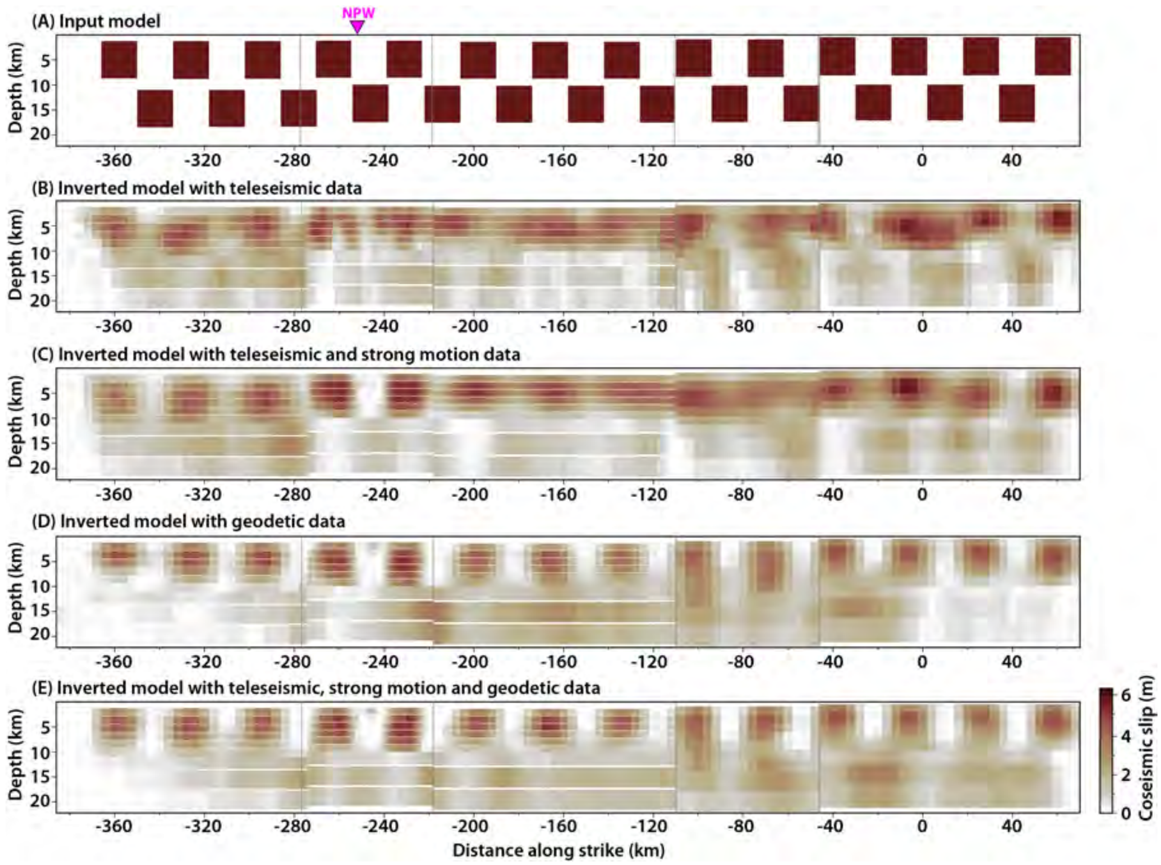

Figure S7. Uniform checkerboard test (Model 2) applied to different datasets. Same as Fig. S6 otherwise.

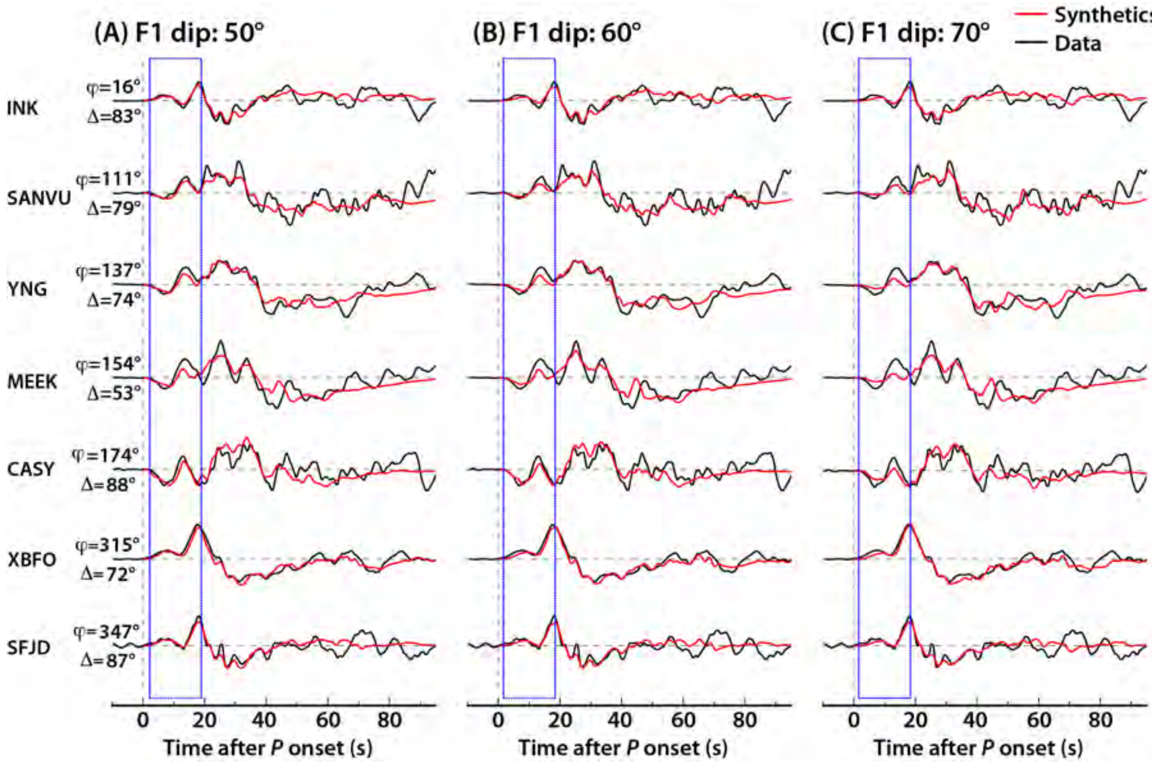

Figure S8. Sensitivity test for different dip angles on subfault F1. (A) 50°. (B) 60°. (C) 70°. All other parameters were kept constant. Station name, azimuth φ, and epicentral distance Δ are shown to the left of each teleseismic *P* waveform. Blue boxes highlight the reduction in early waveform fitting with increasing F1 dip.

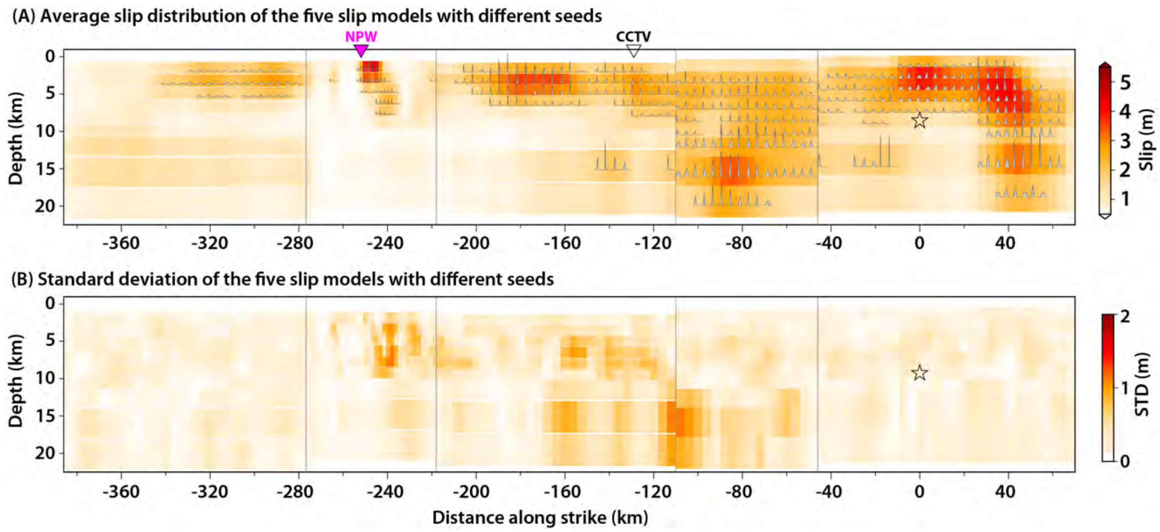

Figure S9. Inversion tests based on different initial seeds for the non-linear optimization. (A) Average slip distribution from five inverted models using different random seeds. The magenta triangle marks station NPW, and the black triangle indicates the CCTV location. (B) Standard deviation of slip distribution from the five inversion models.

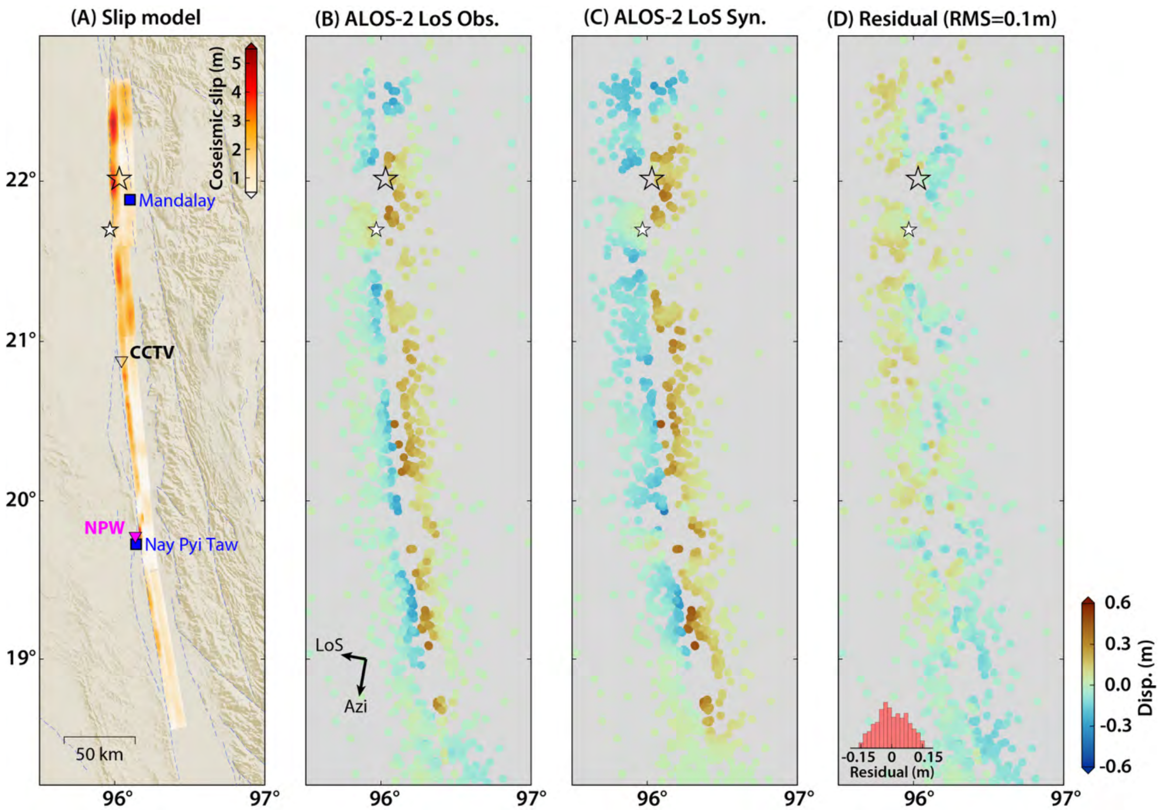

Figure S10. Data fits for the LoS direction displacement derived from the ALOS-2 descending track T041 SAR images. (A) Preferred slip model. (B)-(D) show the observations, synthetics and residuals, respectively. Blue squares indicate the major city locations. Black outline and white stars show the epicenter of the mainshock and M6.7 aftershock, respectively. Magenta and black outline inverted triangles mark the location of station NPW and the CCTV site, respectively. The histogram in (D) illustrates the residual distribution.

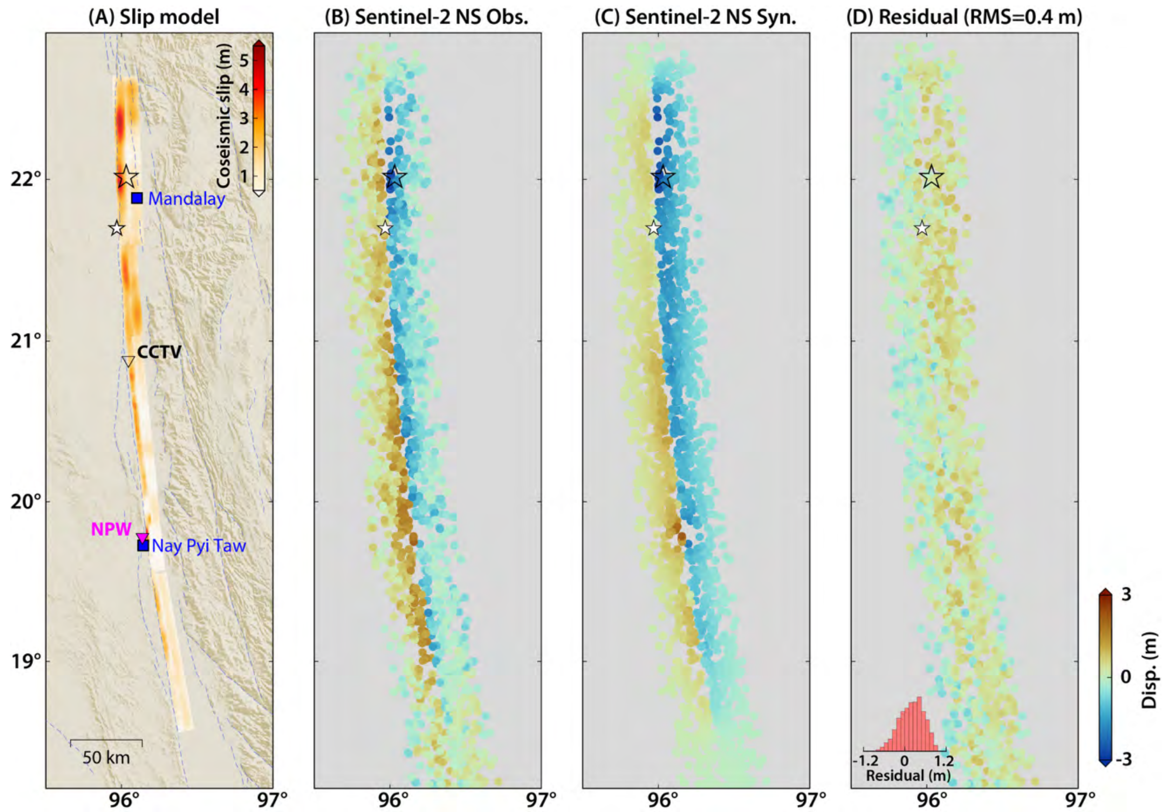

Figure S11. Data fits for the NS direction displacement derived from the Sentinel-2 optical images. (A) Preferred slip model. (B)-(D) show the observations, synthetics and residuals, respectively. Blue squares indicate the major city locations. Black outline and white stars show the epicenter of the mainshock and M6.7 aftershock, respectively. Magenta and black outline inverted triangles mark the location of station NPW station and the CCTV site, respectively. The histogram in (D) illustrates the residual distribution.

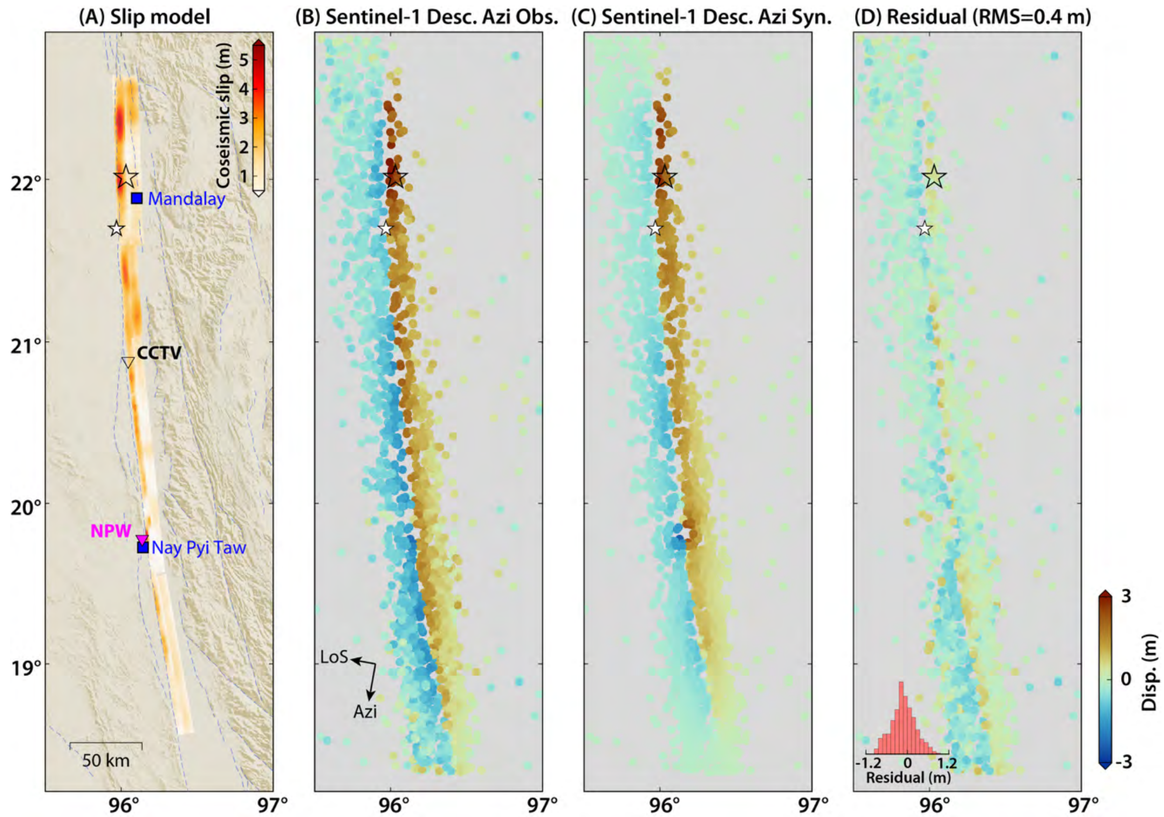

Figure S12. Data fits for the azimuth direction displacement based on the Sentinel-1 descending track T033D and T106D SAR images. (A) Preferred slip model. (B)-(D) show the observations, synthetics and residuals, respectively. Blue squares indicate the major city locations. Black outline and white stars show the epicenter of the mainshock and M6.7 aftershock, respectively. Magenta and black outline inverted triangle mark the location of station NPW and the CCTV site, respectively. The histogram in (D) illustrates the residual distribution.

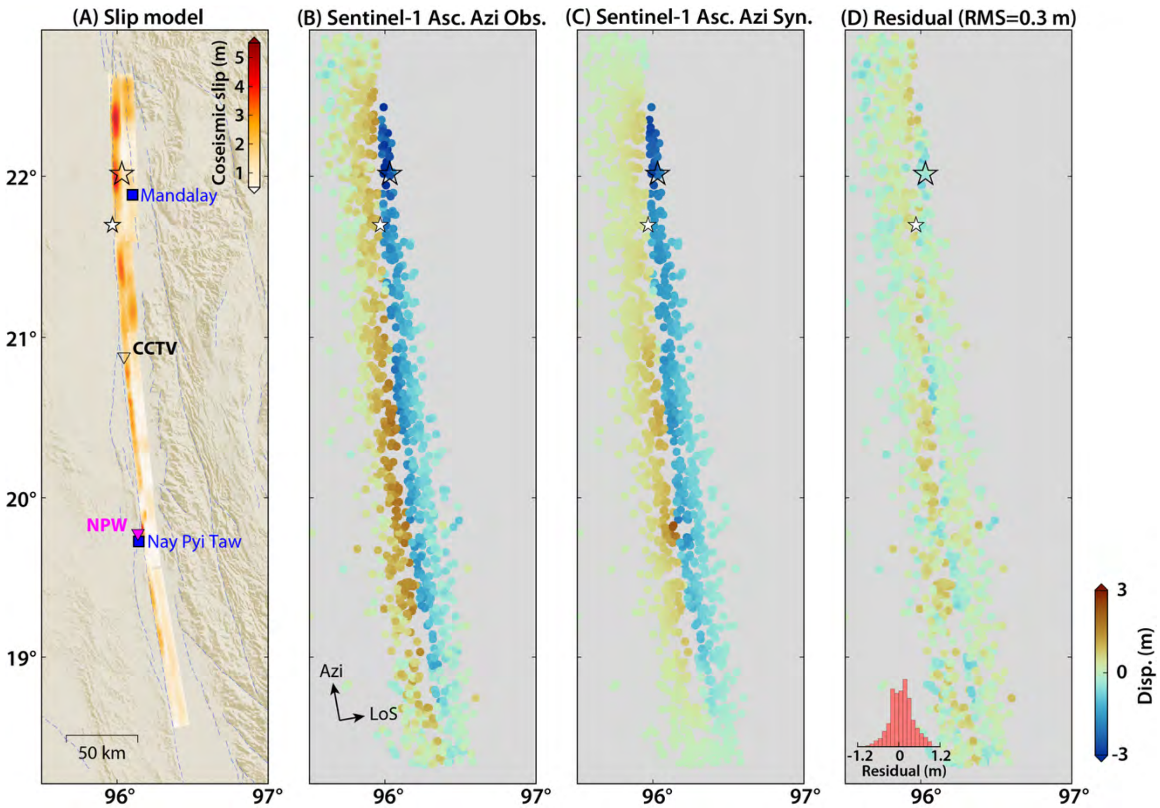

Figure S13. Data fits for the azimuth direction displacement based on the Sentinel-1 ascending track T143A SAR images. (A) Preferred slip model. (B)-(D) show the observations, synthetics and residuals, respectively. Blue squares indicate the major city locations. Black outline and white stars show the epicenter of the mainshock and M6.7 aftershock, respectively. Magenta and black outline inverted triangle mark the location of station NPW station and the CCTV site, respectively. The histogram in (D) illustrates the residual distribution.

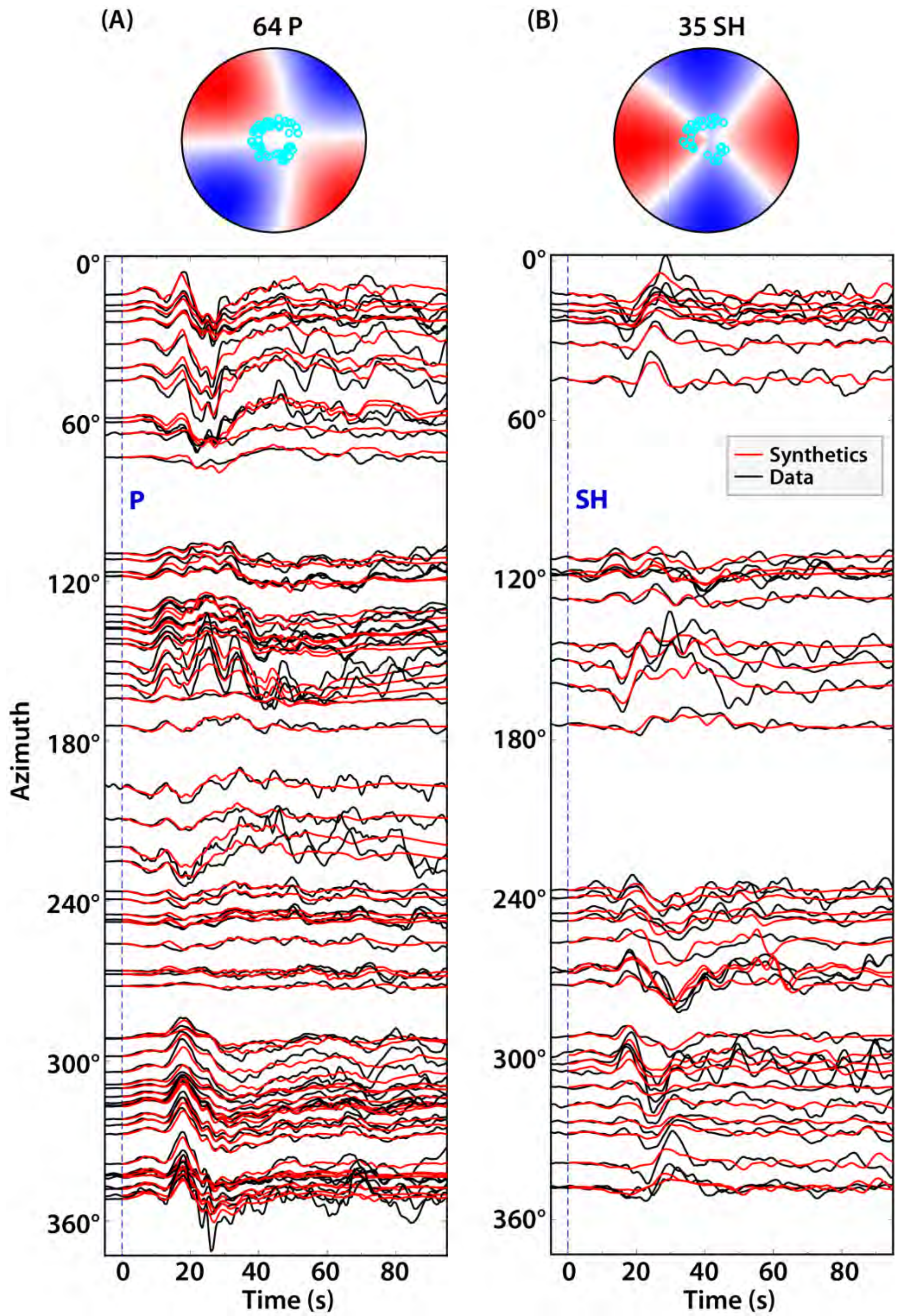

Figure S14. Waveform fits for the teleseismic data for the preferred joint inversion model, including (A) *P*-wave and (B) *SH*-wave. Red and black lines show the normalized synthetic and observed *P*-wave ground displacements and *SH*-wave ground velocities, respectively. The *P*- and *SH*-wave radiation patterns at the top illustrate the takeoff and azimuth angles sampled by the data relative to the radiation nodal planes.

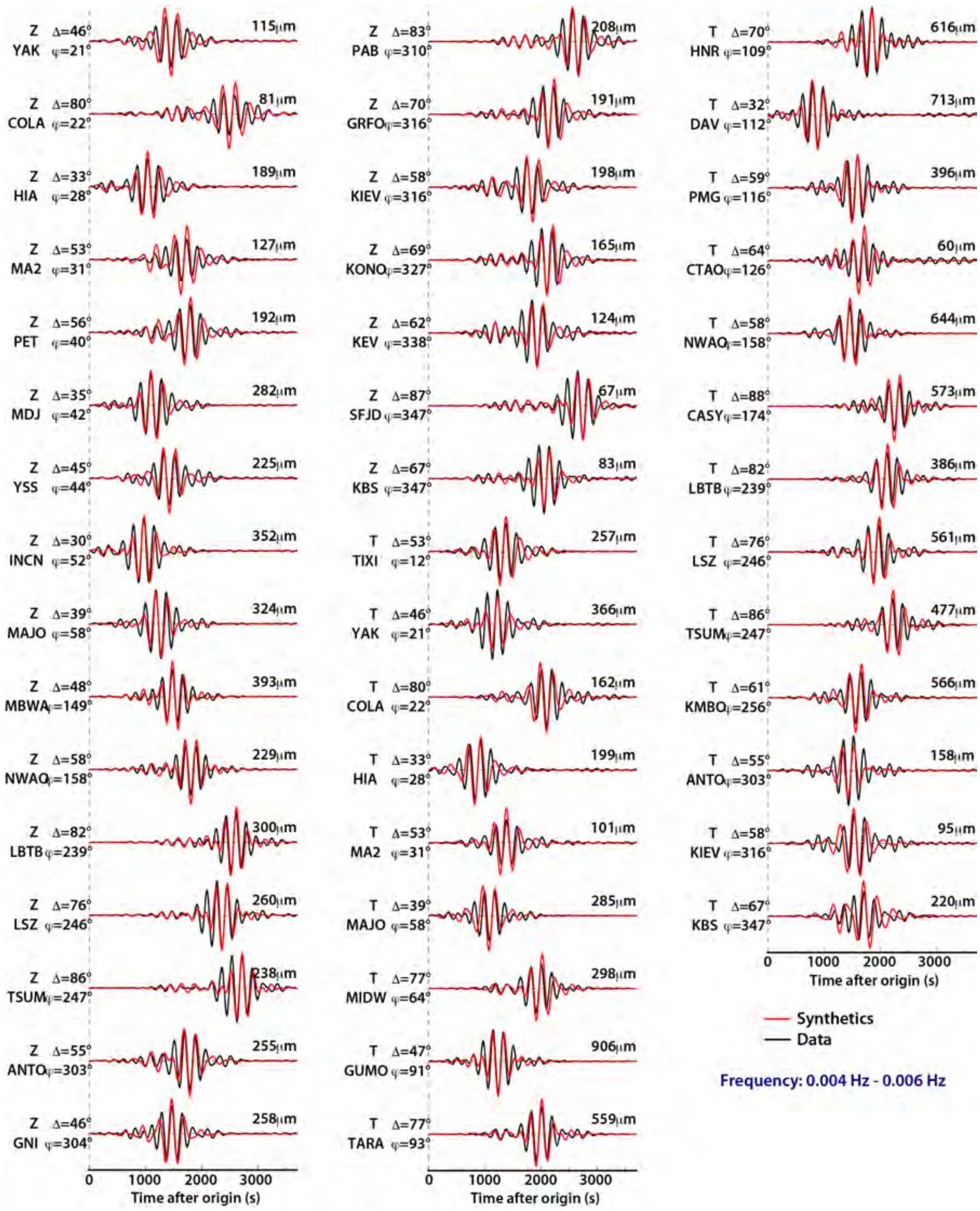

Figure S15. Comparison between the long-period surface wave observations (black) and the predictions for the preferred joint inversion model (red). Both the observed and synthetic waveforms are band-pass filtered between 0.004-0.006 Hz. The left side of each trace shows the component, station name, azimuth φ, and epicentral distance Δ, while the right side indicates the peak amplitude of the observations.

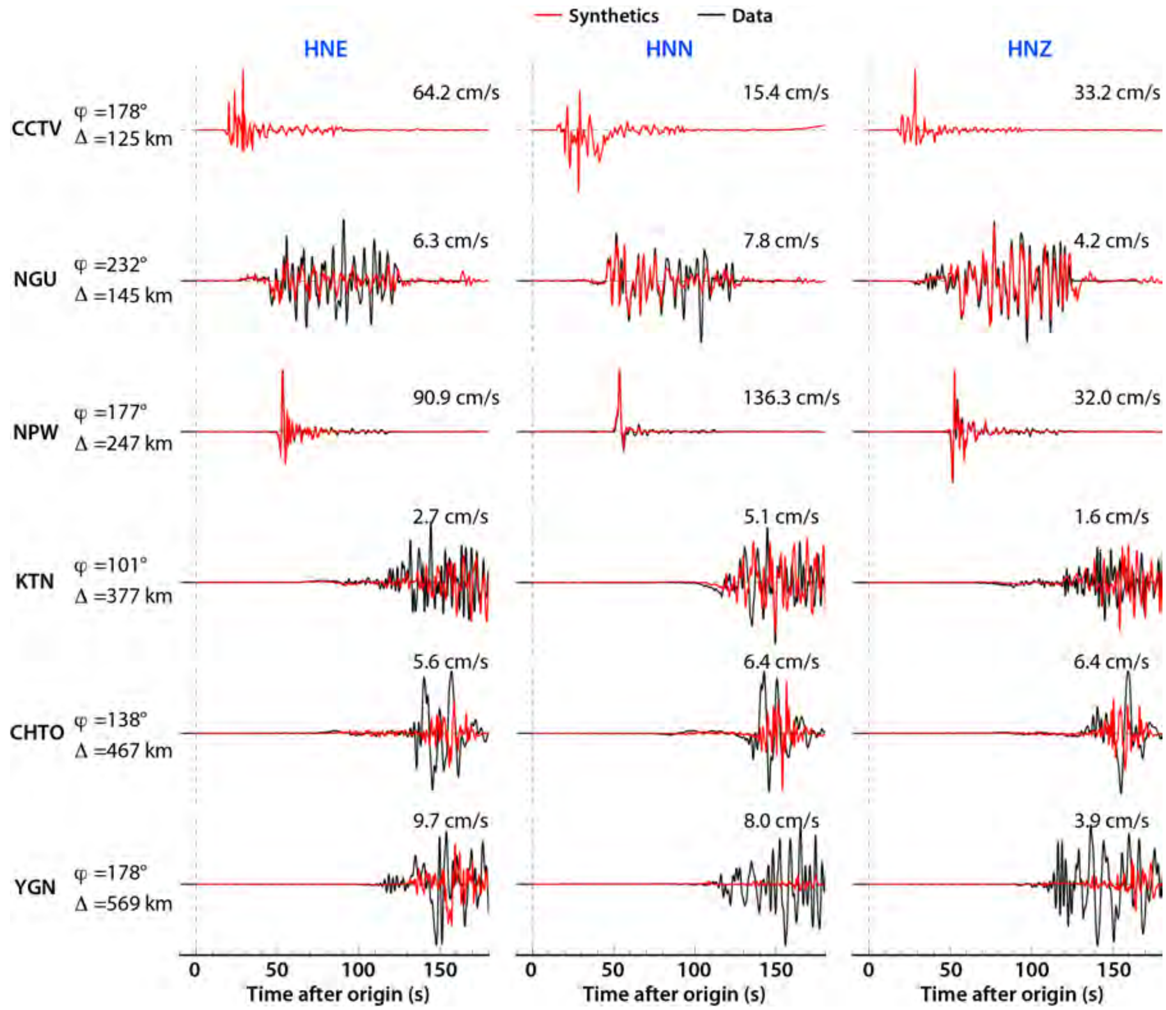

Figure S16. Comparison between the strong motion observations (black) and predictions for the preferred joint inversion (red) for velocity waveforms. A low-pass filter with corner frequency 0.5 Hz is applied once. The left labels show the station names, azimuths φ, and epicentral distances Δ, while the right labels indicate the peak amplitudes of the observations. Only signals from NGU and NPW were used in the joint inversion. Only the prediction for the CCTV site is shown.

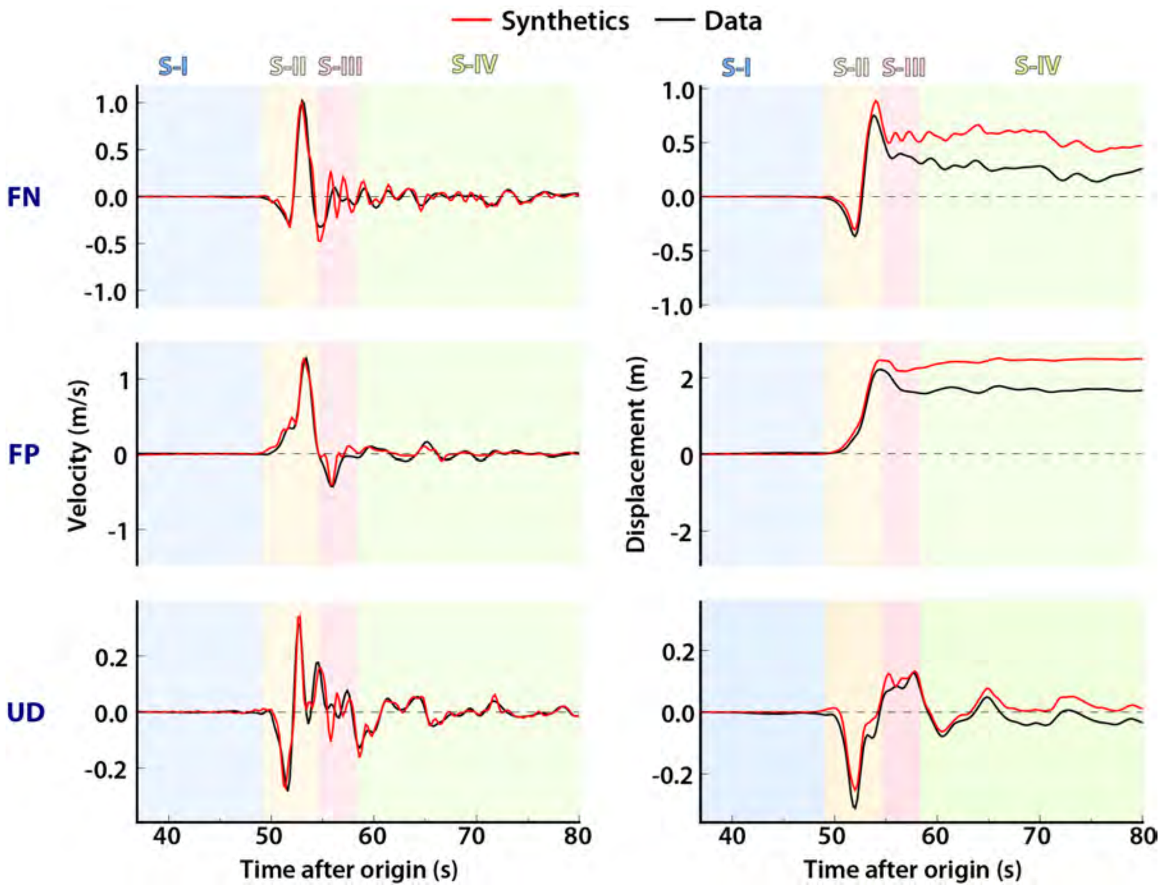

Figure S17. Comparison of velocity and displacement waveforms at station NPW for observations (black) and predictions from the preferred joint inversion model (red). The four stages with distinct waveform characteristics are shown with different background shading, including the early stage S-I, the main pulse stage S-II, the secondary pulse stage S-III, and the tail stage S-IV. Both observed and predicted waveforms were low-pass filtered below 0.5 Hz.

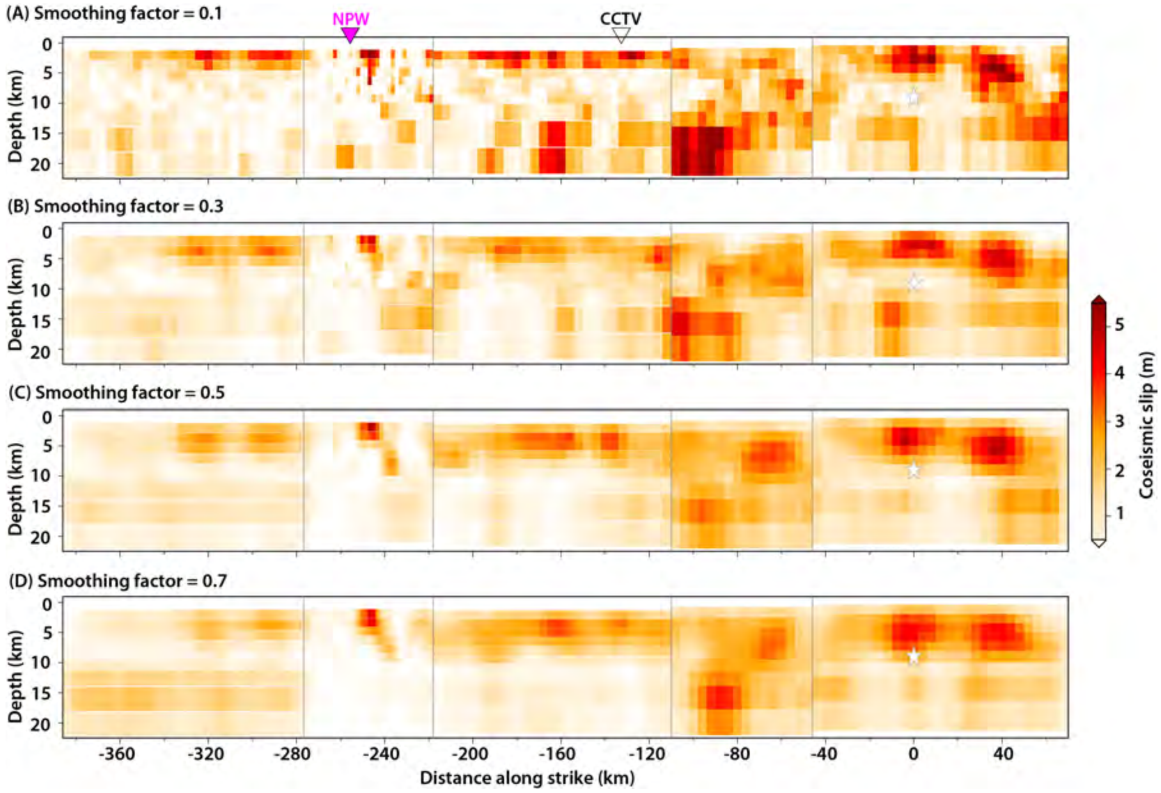

Figure S18. Slip models corresponding to different spatial smoothing factors. (a)-(d) The spatial smoothing factors are 0.1, 0.3, 0.5, and 0.7, respectively. The magenta and black triangles denote the NPW station and the CCTV locations, respectively. The preferred model corresponds to a smoothing factor of 0.5.

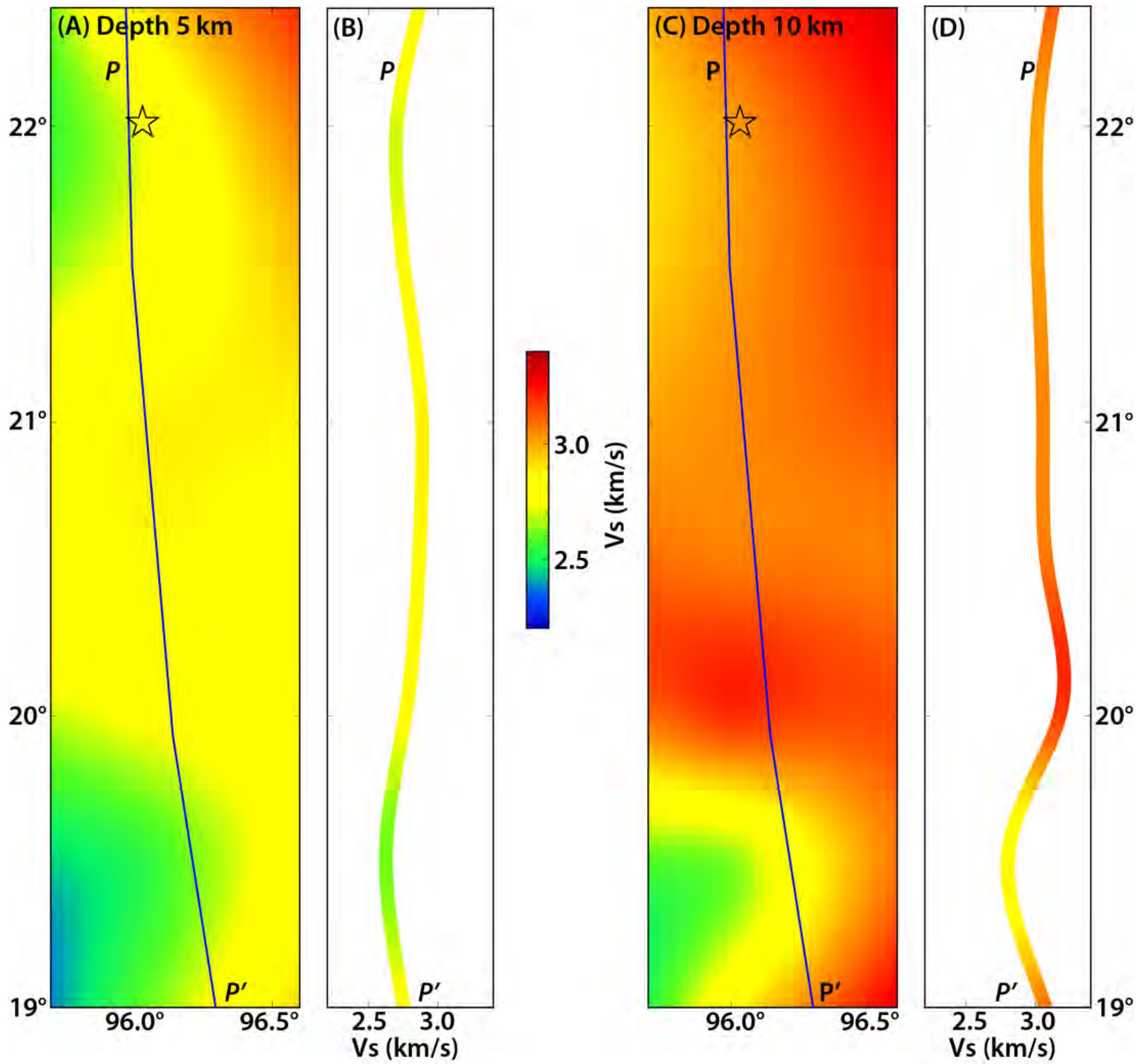

Figure S19. (A) Shear-wave velocity at 5 km depth and (B) its profile along PP'; (C) Shear-wave velocity at 10 km depth and (D) its corresponding profile. *Vs* near the epicenter (black star) are lower than those in the southern fault segment. The velocity model is from Wang et al. (*16*).

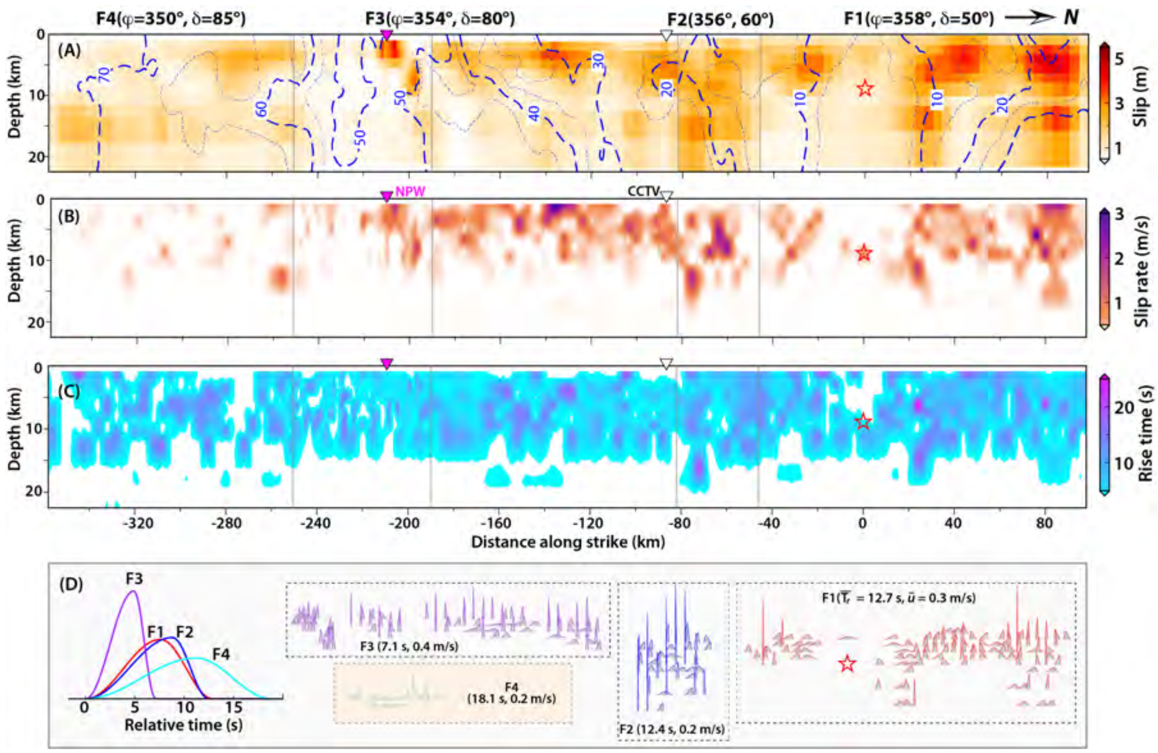

Figure S20. Inverted model using an epicenter shifted ~30 km southward, as estimated by Wei et al. (*1*), with all other inversion parameters identical to those of the preferred model. Other figure layout is the same as in Fig. 3A-C and Fig. 3E.

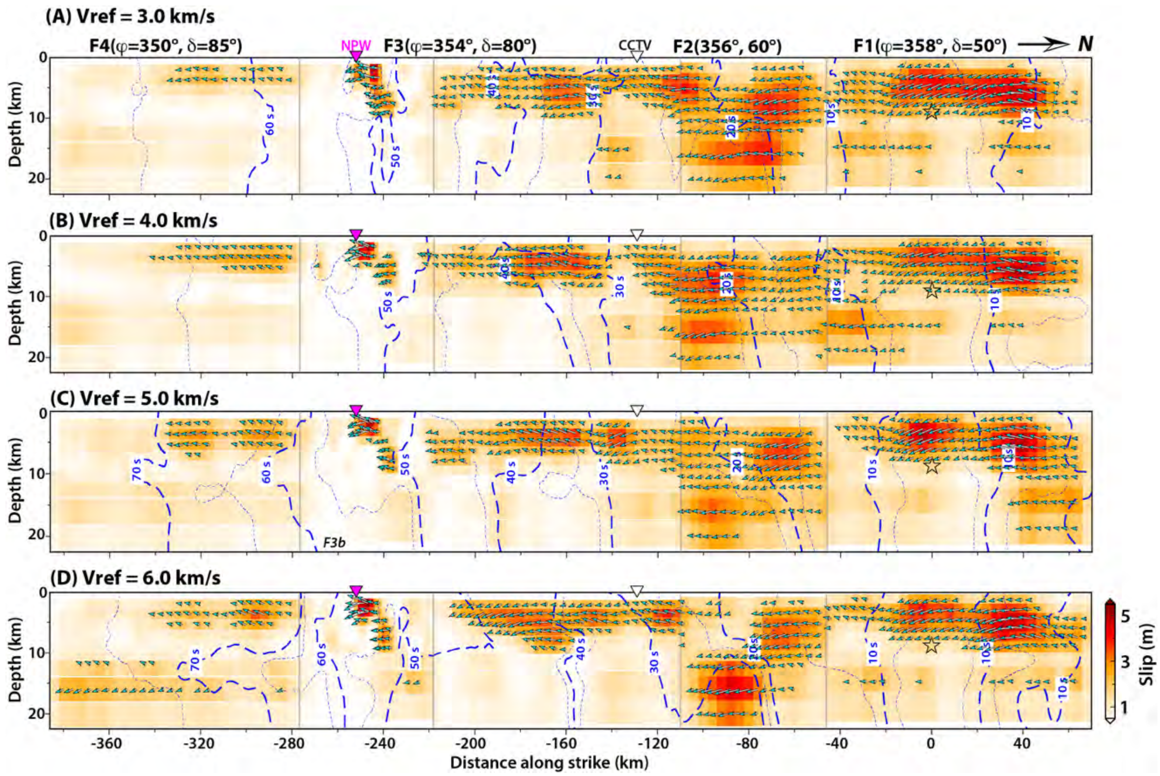

Figure S21. Slip distributions with different reference rupture speeds for the allowed range of speeds of (A) 3.0 km/s, (B) 4.0 km/s, (C) 5.0 km/s, (D) 6.0 km/s. Rupture speed variation occurs in each model with 10 s isochrones (blue curves) indicating position of the rupture front at each time for the models; these indicate similar time evolution of the slip models despite the large difference in reference speed of the models.

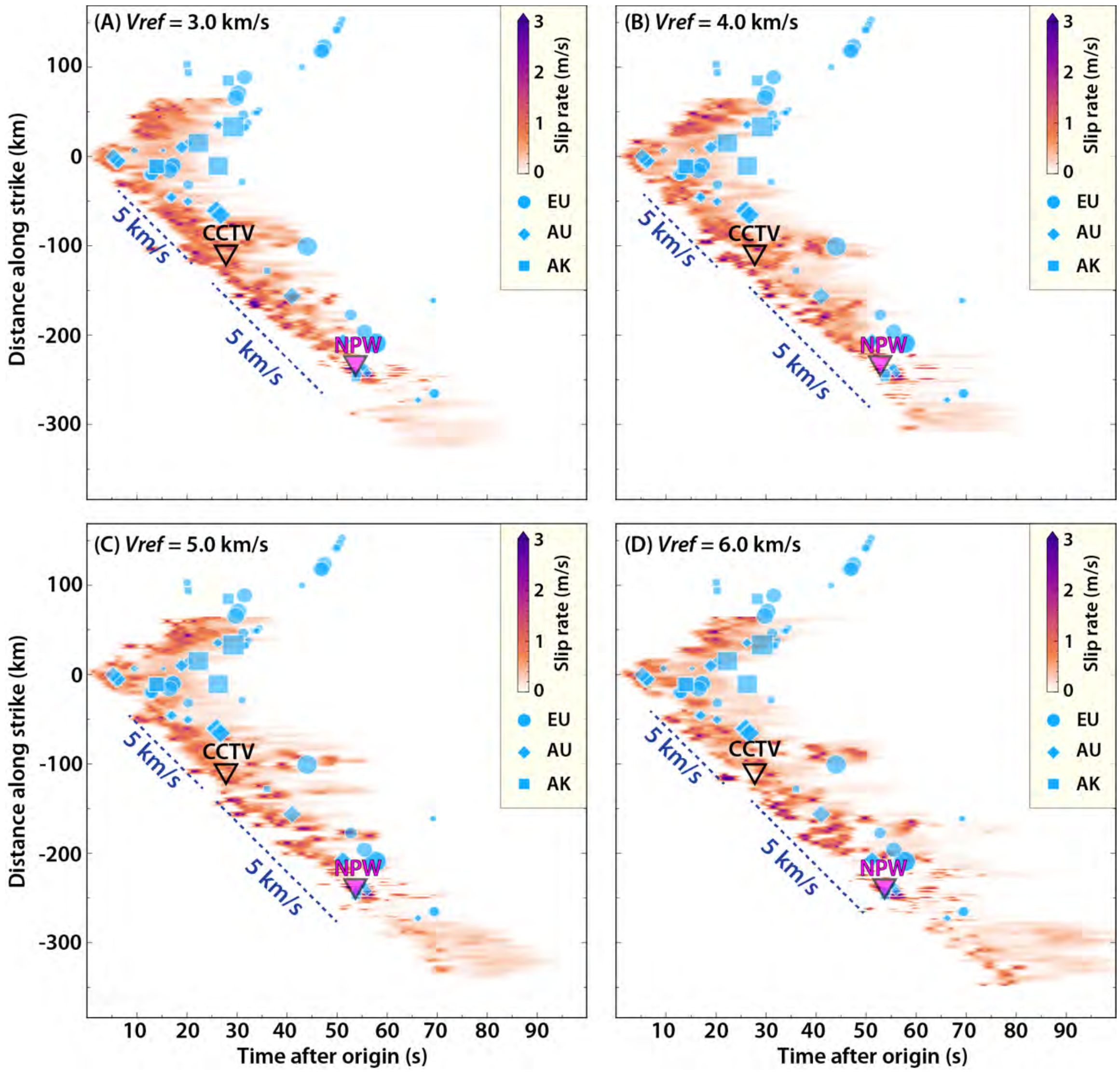

Figure S22. The space-time evolution of slip rate along strike for inversion with different reference rupture speeds. Same as Fig. 5B otherwise.

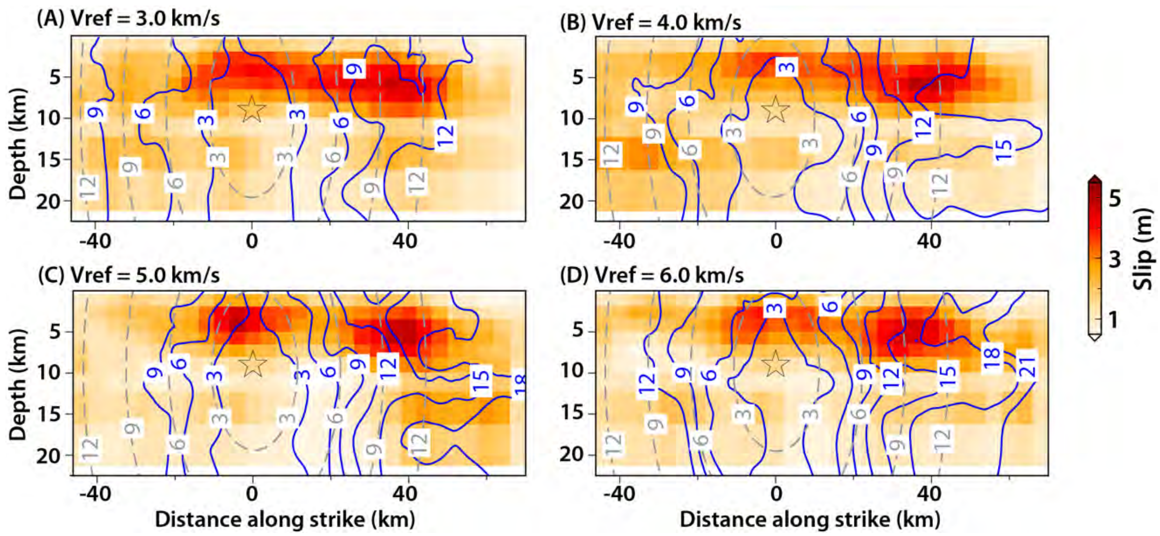

Figure S23. Slip distributions on segment F1 for different reference rupture speeds. Blue dashed and gray contours show the inverted rupture time position and predictions for a constant rupture speed of 3.5 km/s, respectively.

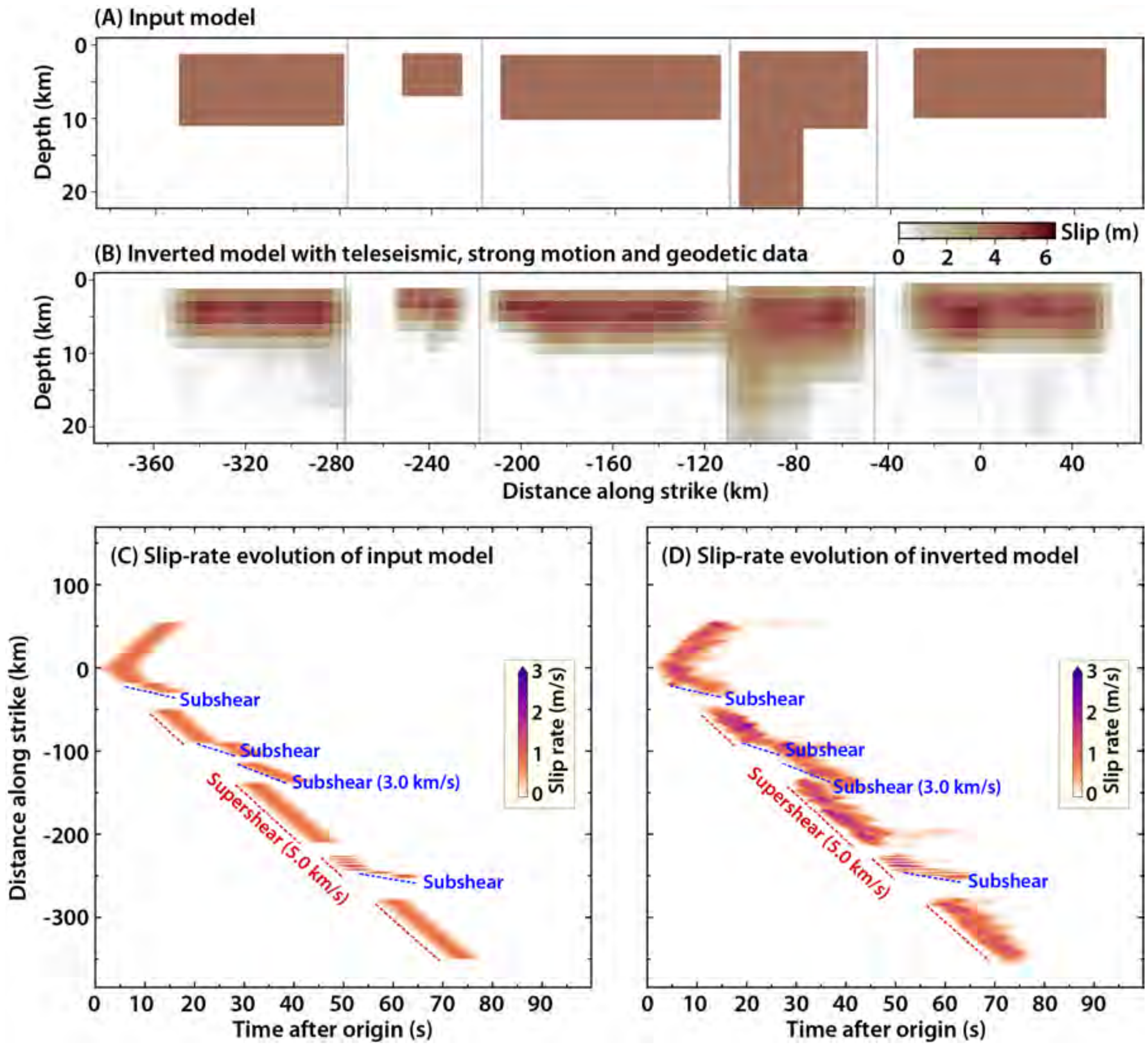

Figure S24. Synthetic rupture-speed resolution test with multiple episodes of intermittent super ruptures. (A, C) Input model and prescribed rupture pattern. (B, D) Inverted model and recovered rupture pattern.

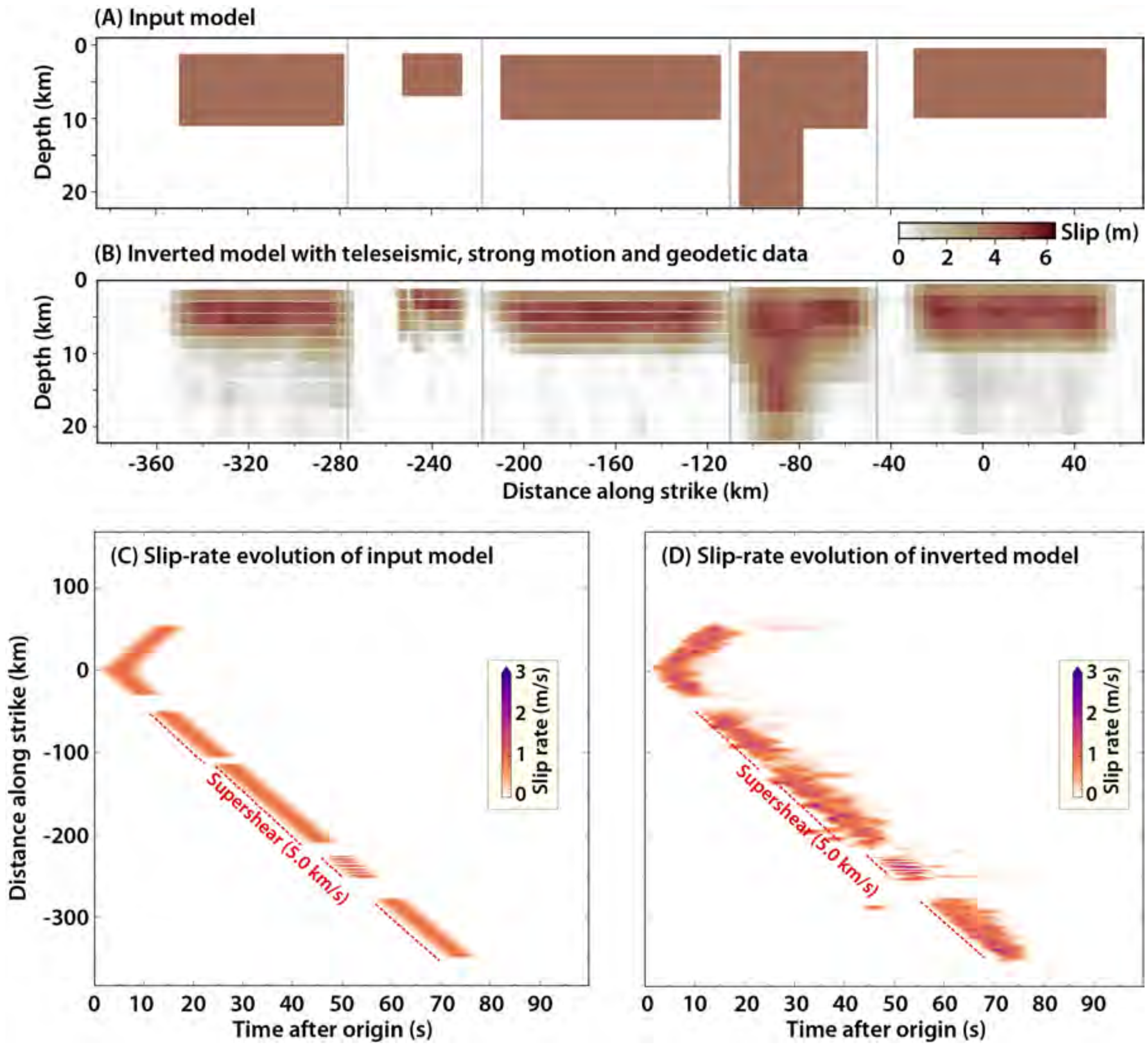

Figure S25. Synthetic rupture-speed resolution test with an assumed sustained supershear rupture. (A, C) Input model and prescribed rupture pattern. (B, D) Inverted model and recovered rupture pattern.

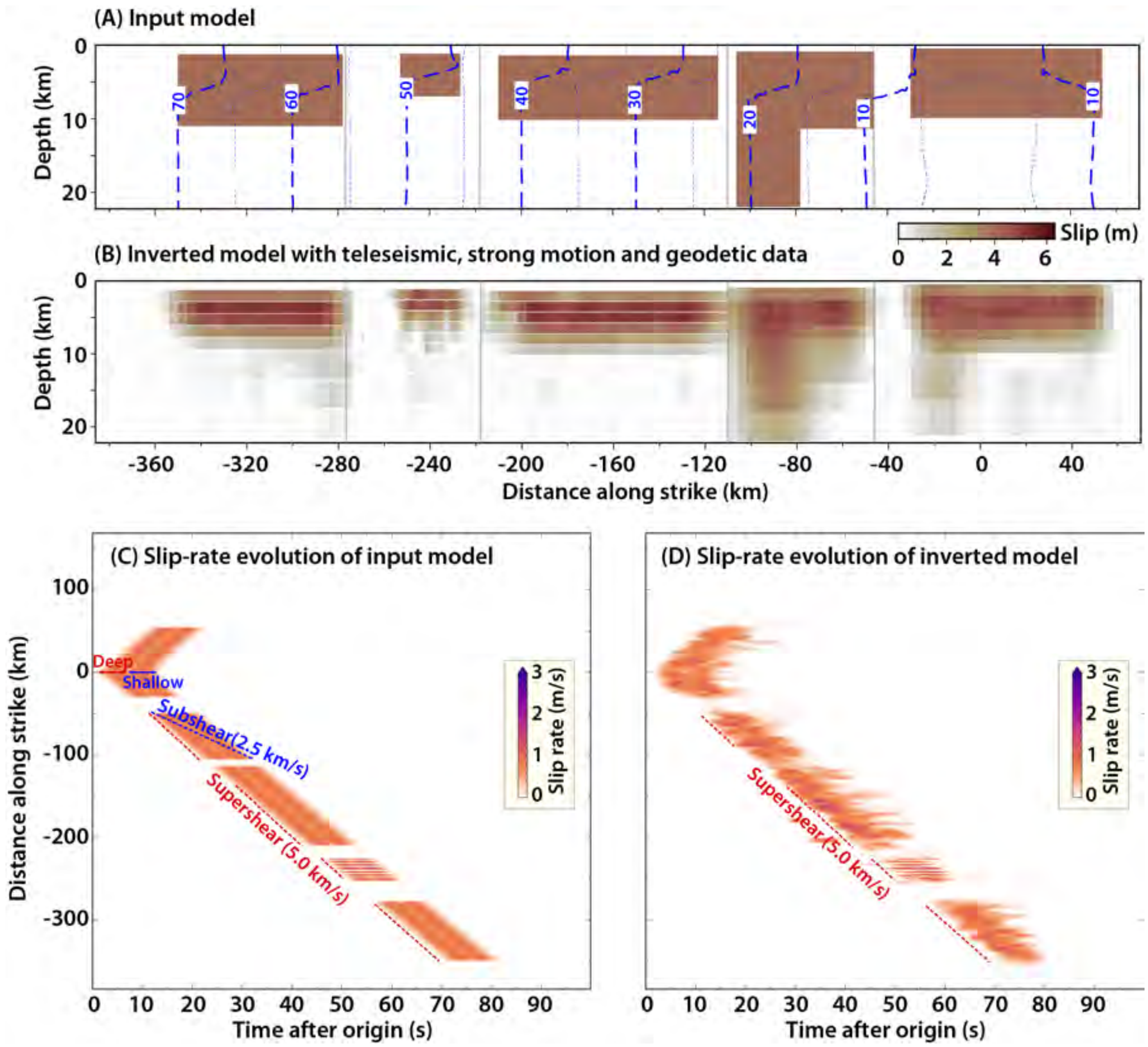

Figure S26. Synthetic rupture-speed resolution test with shallow subshear (2.5 km/s) and deep supershear (5.0 km). (A, C) Input model and prescribed rupture pattern. (B, D) Inverted model and recovered rupture pattern.

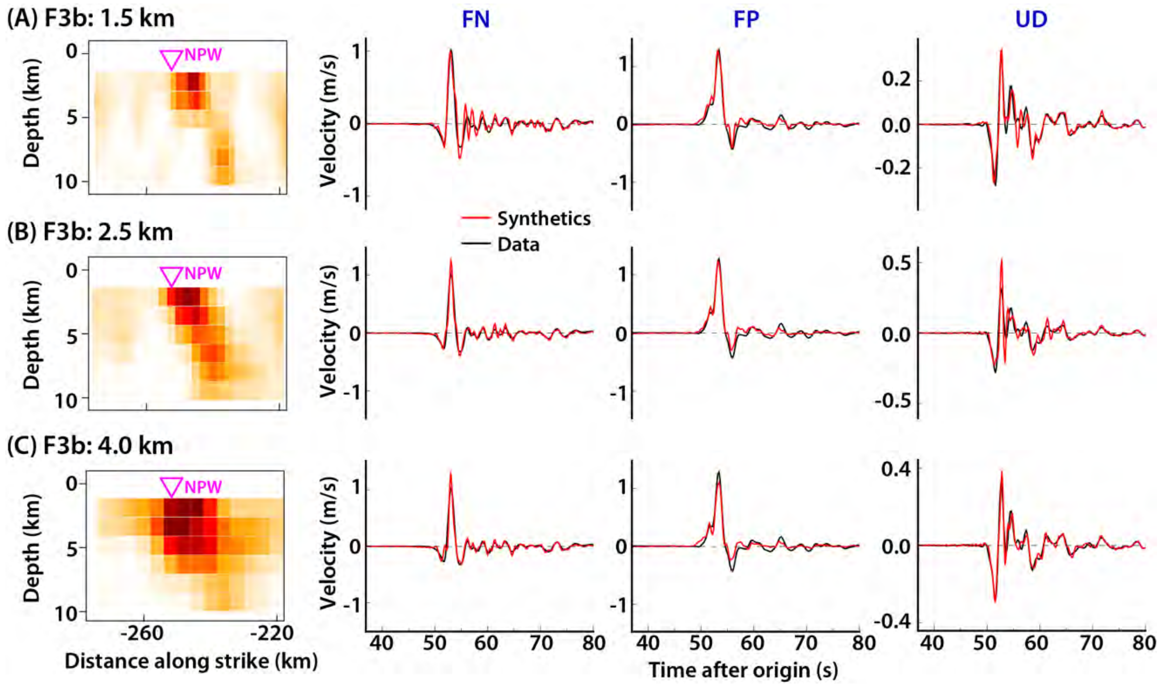

Figure S27. Inverted slip model with different grid sizes on subfault F3b grid sizes and corresponding fit to NPW velocity waveform (FP, FN and UD components). (A) Local inverted slip distribution with along strike grid size of 1.5 km on F3b. (B) Local inverted slip distribution with along strike grid size of 2.5 km on F3b. (C) Local inverted slip distribution with along strike grid size of 4.0 km on F3b. For waveform fitting, red and black lines represent observations and predictions, respectively.

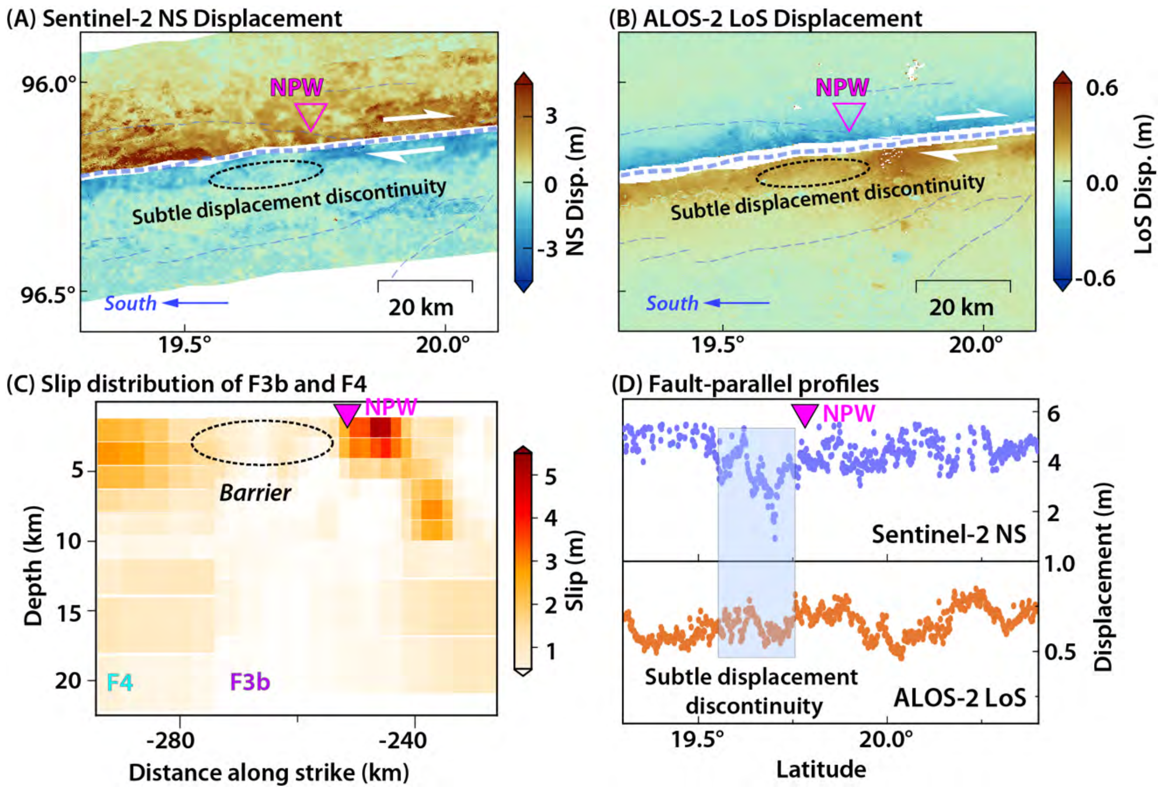

Figure S28. (A) Sentinel-2 north-south localized deformation field near NPW. (B) ALOS-2 LoS localized deformation field near NPW. Inverted triangle marks station NPW, black dashed ellipse indicates discontinuous displacement, thick and thin light-blue dotted lines are Sagaing fault and other regional faults. White arrow indicates relative motion across the fault. (C) Slip distribution of F3b and F4 segments. Black dotted ellipse indicates an inferred rupture barrier. (D) Fault parallel profiles of Sentinel-2 NS (light blue dots) and ALOS-2 LoS (orange dots) displacement field. The shadowed box highlights the displacement discontinuity (reduction) indicated in (A) and (B).

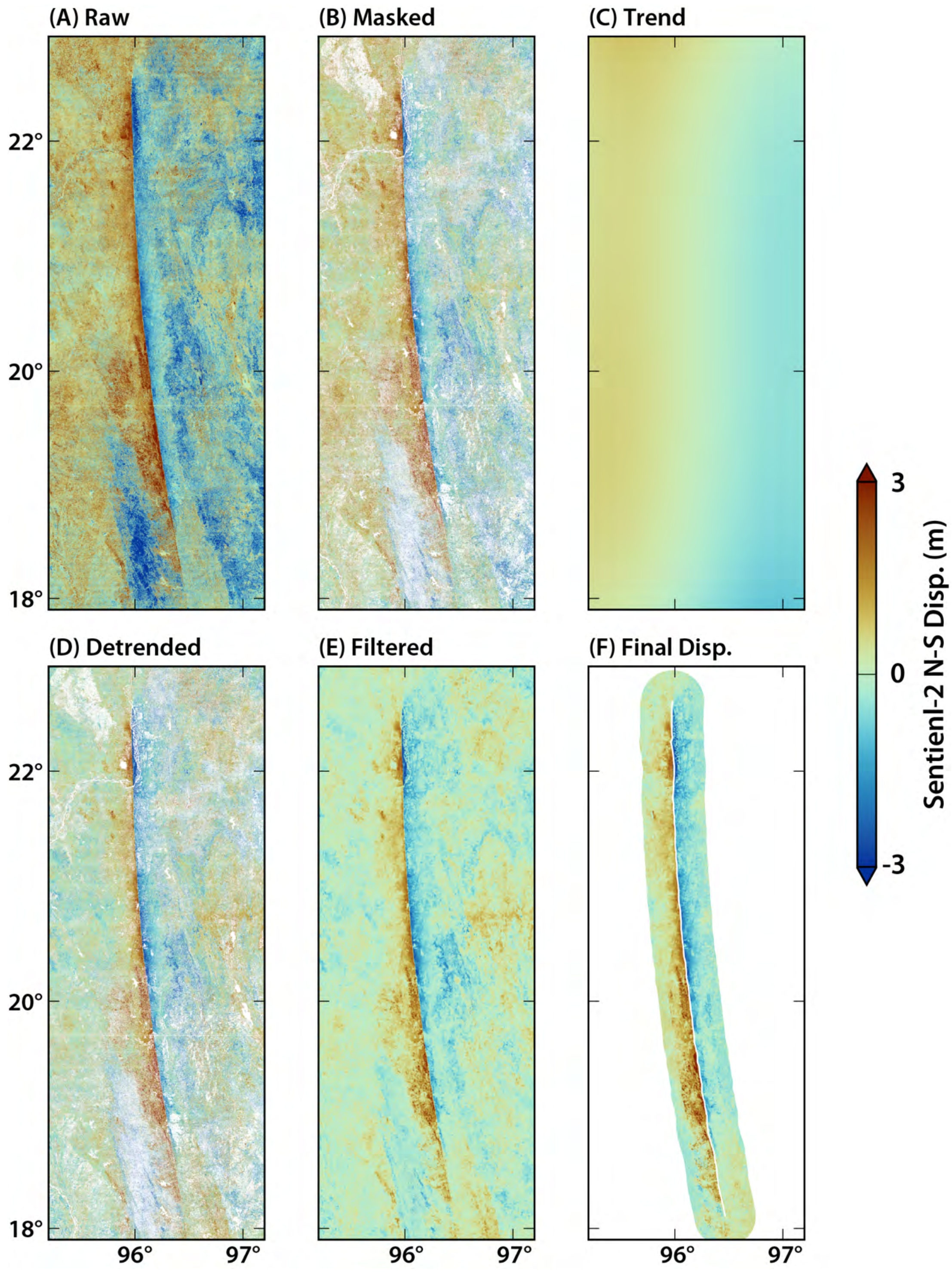

Figure S29. Post-processing workflow for the 2025 Myanmar earthquake N-S surface deformation field based on Sentinel-2 images. (A) Original cross-correlation deformation field. (B) Deformation field after applying a coherence mask. (C) Trend obtained by polynomial fitting. (D) Deformation field after trend removal. (E) Deformation field after filtering. (F) Final deformation field after resampling and cutting.

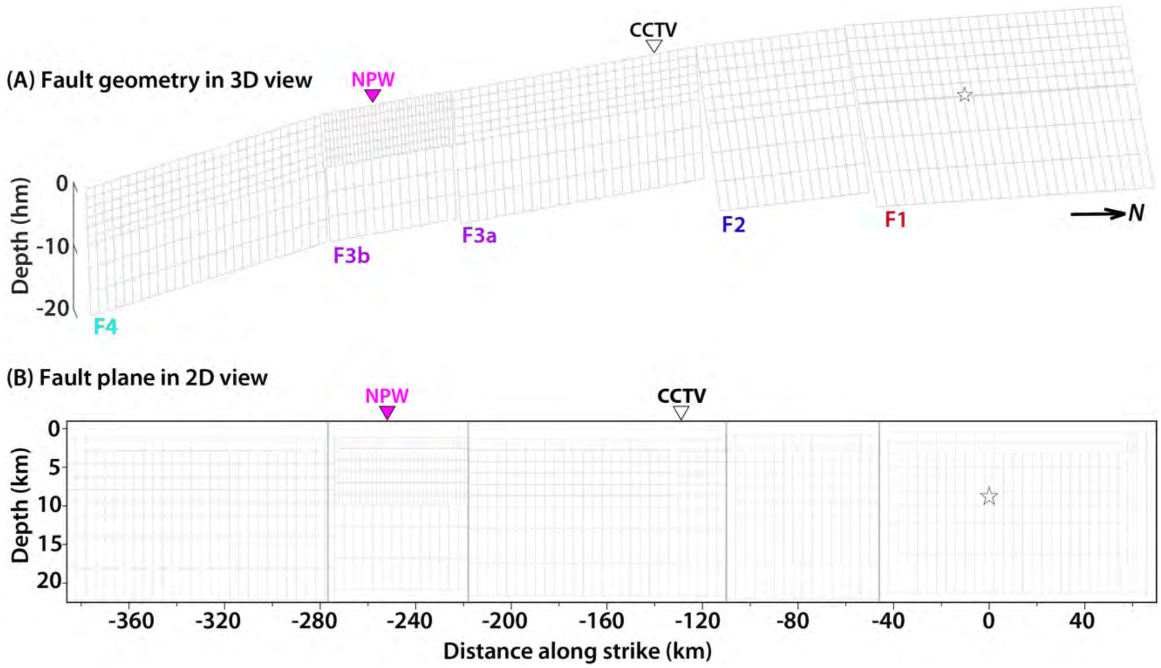

Figure S30. Constructed fault model geometry. (a) Fault geometry in three-dimensional view. (b) Fault plane in two-dimensional view, with grid sizes varying along strike and dip directions. Black star marks the hypocenter. Black and magenta inverted triangles indicate the CCTV site and station NPW, respectively.

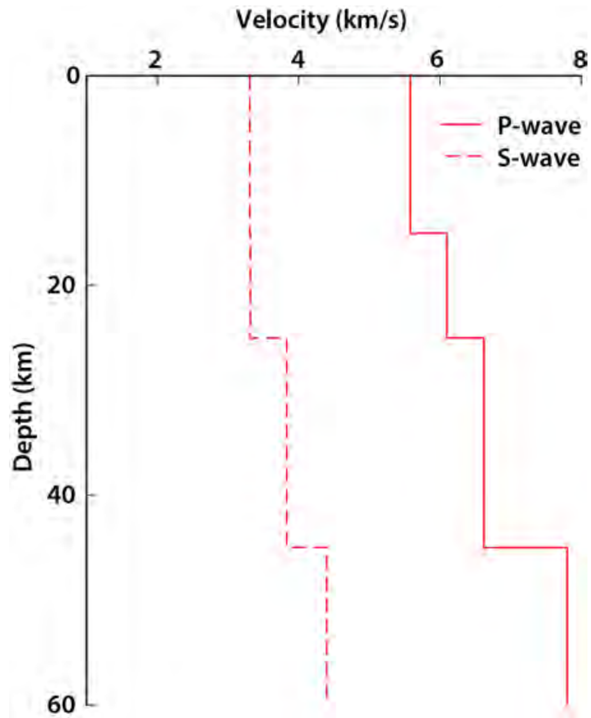

Figure S31. The regional velocity model used in this study (*17*). Solid lines represent *P*-wave velocity, and dashed lines represent *S*-wave velocity.

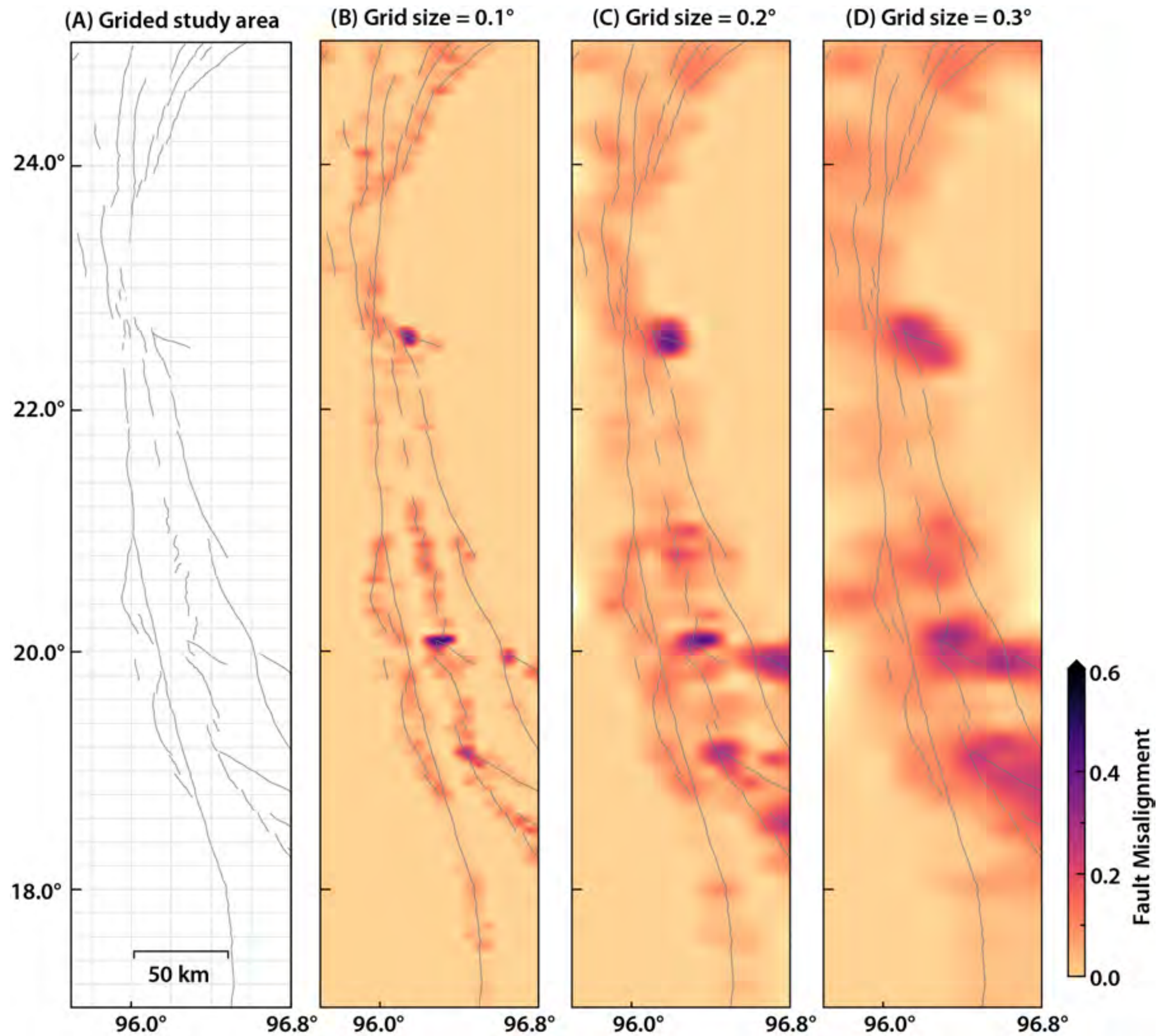

Figure S32. (A) Gridded study area with a grid size of 0.2°. (B)-(D) Fault misalignment field obtained for grid sizes of 0.1°, 0.2°, and 0.3°, respectively. Thin grey lines indicate surface fault traces.

Table S1. SAR data used in the study

Data	Track	Date of master	Date of slave	Direction	Band
Sentinel-1A	T033D	2025/03/19	2025/03/31	Descending	C
Sentinel-1A	T106D	2025/03/24	2025/04/05	Descending	C
Sentinel-1A/C	T143A	2025/03/27	2025/04/02	Ascending	C
ALOS-2	T041D	2025/02/16	2025/03/30	Descending	L

Table S2. Sentinel-2 optical image data used in the study

Time window	satellite	Date	Strip number	Track
Pre-seismic	S2C	2025/03/02	T46QHD	R004
	S2C	2025/03/02	T46QHE	R004
	S2C	2025/03/02	T46QHF	R004
	S2C	2025/03/02	T46QHG	R004
	S2C	2025/03/02	T46QHH	R004
	S2C	2025/03/05	T46QGG	R047
	S2C	2025/03/05	T46QGH	R047
	S2C	2025/03/05	T46QGJ	R047
	S2C	2025/03/05	T46QGK	R047
	S2C	2025/03/05	T46QGL	R047
Post-seismic	S2C	2025/04/01	T46QHD	R004
	S2C	2025/04/01	T46QHE	R004
	S2C	2025/04/01	T46QHF	R004
	S2C	2025/04/01	T46QHG	R004
	S2C	2025/04/01	T46QHH	R004
	S2C	2025/04/04	T46QGG	R047
	S2C	2025/04/04	T46QGH	R047
	S2C	2025/04/04	T46QGJ	R047
	S2C	2024/04/04	T46QGK	R047
	S2C	2025/04/04	T46QGL	R047

Table S3. Inversion parameters used in the study

Segments	Size of deep (km × km)	Size of shallow (km × km)	Strike	Dip	Rake	Slip (m)	Length (km)
F1	4.0 × 5.0	4.0 × 2.0	358°	50°	160°-200°	(0, 7)	115
F2	4.0 × 5.0	4.0 × 2.0	356°	60°	170°-190°	(0, 7)	63
F3a	4.0 × 5.0	4.0 × 2.0	354°	80°	160°-200°	(0, 7)	107
F3b	4.0 × 5.0	1.8 × 1.5	354°	80°	160°-200°	(0, 7)	57
F4	4.0 × 5.0	4.0 × 2.0	350°	85°	160°-200°	(0, 7)	111

Table S4. Weights of different datasets used in the joint inversion

<table>
<tr><th>Dataset</th><th colspan="30">Weight</th></tr>
<tr><td>Teleseismic P-wave</td><td colspan="30">1.0</td></tr>
<tr><td>Teleseismic SH-wave</td><td colspan="30">0.5</td></tr>
<tr><td>Long-period surface wave</td><td colspan="30">2.0</td></tr>
<tr><td rowspan="2">Strong motion wave</td><td colspan="6">NPW</td><td colspan="6">NGU</td><td colspan="6">KTN</td><td colspan="6">CHTO</td><td colspan="6">YGN</td></tr>
<tr><td colspan="6">16.0</td><td colspan="6">4.0</td><td colspan="6">0.0</td><td colspan="6">0.0</td><td colspan="6">0.0</td></tr>
<tr><td rowspan="2">Geodetic data</td><td colspan="10">Sentinel-2</td><td colspan="10">ALOS-2</td><td colspan="10">Sentiel-1A/C</td></tr>
<tr><td colspan="10">2.0</td><td colspan="10">2.0</td><td colspan="10">0.5</td></tr>
</table>

Reference

1. S. Wei *et al.* Supershear rupture sustained through a thick fault zone in the 2025 M_W 7.8 Mandalay earthquake. *Science*. **390**, 468-475 (2025).
2. L. Ye, T. Lay, H. Kanamori. The 28 March 2025 M_W 7.8 Myanmar earthquake: Preliminary analysis of an ~480 km long intermittent supershear rupture. *The Seismic Record*. **5**, 260-269 (2025).
3. N. Inoue *et al*. A multiple asymmetric bilateral rupture sequence derived from the peculiar teleseismic *P*-waves of the 2025 Mandalay, Myanmar earthquake. *Seismica*. **4**, 1 (2025).
4. D. Melgar *et al.* Supershear source model of the 2025 M_W 7.8 Myanmar earthquake and paleoseismology of the Sagaing Fault: regions of significant overlap with past earthquakes. *Seismica*. **4**, 2 (2025).
5. L. Xu *et al*. Bimaterial effect and favorable energy ratio enabled supershear rupture in the 2025 Mandalay earthquake. *Science*. **390**, 476-481 (2025).
6. D. E. Goldberg *et al*. Ultralong, supershear rupture of the 2025 M_W 7.7 Mandalay earthquake reveals unaccounted risk. *Science.* **390**, 458-462 (2025).
7. B. Li *et al*. Seismic gap breached by the 2025 M_W 7.7 Mandalay (Myanmar) earthquake. *Nat. Geosci.* **18**, 1-9 (2025).
8. S. L. Antoine *et al*. The 2025 M_W 7.7 Mandalay, Myanmar, earthquake reveals a complex earthquake cycle with clustering and variable segmentation on the Sagaing Fault. *Proc. Natl. Acad. Sci. U.S.A*. **122**, 33, e2514378122 (2025).
9. Y. Li *et al*. Sustained supershear rupture during the 2025 Mandalay, Myanmar earthquake. *Commun. Earth Environ*. **6**, 1030 (2025).
10. E. O. Lindsey *et al*. Mature fault mechanics revealed by the highly efficient 2025 Mandalay earthquake. *Nat. Commun.* **16**, 10937 (2025).
11. X. Qiao *et al*. Coseismic slip and early rapid afterslip of the 2025 M_W 7.7 Myanmar earthquake constrained by space-based geodetic observations. *Geophys. Res. Lett.* **52**, 22, e2025GL118226 (2025).
12. F. Vera *et al.* Supershear rupture along the Sagaing fault seismic gap: The 2025 Myanmar earthquake. *The Seismic Record.* **5**, 289-299 (2025).
13. S. Hirano, R. Doke, T. Maeda. Supershear-subshear-supershear rupture sequence during the 2025 Mandalay earthquake in Myanmar. *Seismica*. **4**, 2 (2025).
14. Q. Yao, C. Yu, M. Zhou. Bilateral supershear rupture of the 2025 M_W 7.7 Myanmar earthquake imaged by global *P*-wave and regional surface-wave back-projections. *Geophys. Res. Lett*. **52**, 20, e2025GL116800 (2025).
15. S. T. Lai *et al*. Capacity building enables unique near-fault observations of the destructive 2025 M_W 7.7 Myanmar earthquake. *Earth Syst. Sci. Data*. **17**, 5149-5164 (2025).
16. X. Wang *et al*. A 3-D shear wave velocity model for Myanmar region. *J. Geophys. Res.: Solid Earth*. **124**, 504-526 (2019).
17. H. A. Shiddiqi, P. P. Tun, L. Ottemöller. Minimum 1D velocity model and local magnitude scale for Myanmar. *Seismol. Res. Lett.* **90**, 1923-1936 (2019).